Two-photon photoemission spectroscopy of image states

Thomas Fauster and Wulf Steinmann
Sektion Physik, Universität München, Schellingstrasse 4, D-80799 München, Germany
(August 31, 1994)

Preprint of article published in:

Electromagnetic Waves: Recent Developments in Research
Volume 2: Photonic Probes of Surfaces Chapter 8, pp. 347–411
Editor: P. Halevi Elsevier (Amsterdam) 1995

In two-photon photoemission a photon from a pulsed laser excites an electron from a state below the Fermi level to an unoccupied intermediate state below the vacuum level. A second photon ionizes the intermediate state. The energy distribution of the photoelectrons yields information on the energetic position and the lifetime of the intermediate state. Image states are bound states of electrons in front of metal surfaces in the potential well, built by the image potential and the surface. They have been studied extensively by two-photon photoemission. Experimental results on the binding energies of image states on (111) and (100) surfaces of Ag, Au, Cu, and Pd agree with calculations by a one-dimensional scattering model. The results for Fe, Co, and Ni are not yet understood. Lifetimes of image states between 4 and 180 fs have been measured. Particular emphasis is placed on image states on metal overlayers. Information on film growth and surface morphology has been obtained. Lateral localization and coupling to quantum well states has been observed. Dielectric overlayers have also been investigated.

1. INTRODUCTION

Electronic states in solids and at solid surfaces have been studied extensively and comprehensively by photoemission measurements [*Kevan (1992)*]. The process is depicted in the left-hand scheme of Fig. 1. If the photon energy $h\nu$ is known and the kinetic energy E_{kin} of the photoelectron is measured, the energy of the initial state E_i with respect to the vacuum energy E_{vac} can be determined. If the work function $\Phi = E_{vac} - E_F$ is known, the more interesting information on E_i relative to the Fermi level E_F can be obtained. The photoelectron spectrum, i. e., the energy distribution curve is a picture of the density of the initial states, provided the final states form a smooth continuum and the transition probability is homogeneous.

This method of investigating the electronic structure has been developed and refined over the last thirty years to great perfection. Atomically clean surfaces are needed because the escape depth of the photoelectrons is usually only a few monolayers. The escape depth depends on the kinetic energy and, therefore, on the photon energy for a given initial state. Synchrotron radiation as a continuum source in the vacuum ultraviolet has, among many other advantages, offered the possibility of distinguishing surface and bulk effects by scanning the photon energy. Angle-resolved photoelectron spectroscopy yields information about the k vector of the initial state. With monocrystalline samples and well-defined and ordered surfaces it is possible to determine the electronic band structure in particular at high symmetry points and lines of the Brillouin zone.

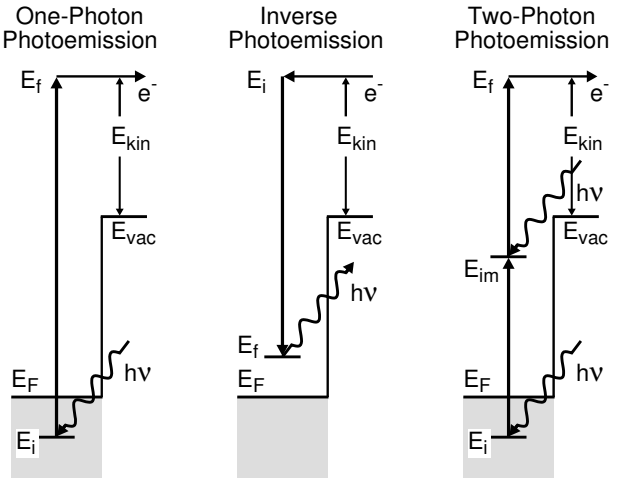

FIG. 1. Schematic energy diagrams for photoemission, inverse photoemission, and two-photon photoemission. The shaded areas indicate the occupied states below the Fermi level E_F of the metal. The kinetic energy E_{kin} of the electron leaving or impinging on the surface is measured relative to the vacuum energy E_{vac}.

The energy range accessible to photoelectron spectroscopy is obviously limited to initial states below E_F and to final states above E_{vac}. Most information obtained by photoemission relates to occupied states below E_F. Results pertaining to final states are scarce and far from complete. In order to investigate the unoccupied states, particularly the range between E_F and E_{vac}, one has to use other methods [*Fuggle and Inglesfield (1992)*]. The most general and widely used is inverse photoemission. The process is shown in the center part of Fig. 1. It is simply the time reversal of the photoemission process. The kinetic energy and the angle of incidence of the impinging electron are chosen and the energy of the photon emitted is measured. The method almost perfectly complements photoemission; the main disadvantage is the limited energy resolution which is inferior to photoemission by more than an order of magnitude. Energy resolution in photoemission is generally limited by the energy analyzer; a resolution of a fraction of a tenth of an eV is quite easily achieved. In inverse photoemission the energy distribution of the incoming electrons – typically several hundred meV – limits the energy resolution. Wherever a better resolution is necessary or desirable in the investigation of unoccupied electronic states, one has to search for an alternative to inverse photoemission.

Two-photon photoemission [*Giesen et al. (1985), Steinmann (1989)*] offers the required combination of high resolution and applicability to the range between E_F and E_{vac}. The process is demonstrated in the right-hand scheme of Fig. 1. In this chapter we describe the process of two-photon photoemission, the experimental considerations and requirements, and the application of the method to the study of image states. They constitute a special type of electronic states in front of rather than at metal surfaces.

2. TWO-PHOTON PHOTOEMISSION

1. Spectroscopy

1. Monochromatic and bichromatic mode

In two-photon photoemission (2PPE, as it will be designated from here on for the sake of brevity and convenience) the first photon excites an electron from the initial state E_i to an intermediate state E_{im}, from where a second photon brings the electron to the final state above E_{vac} (see right-hand part of Fig. 1). Obviously E_{im} has to be below E_{vac} in order to avoid one-photon photoemission which would completely obscure the 2PPE signal. A more stringent condition for this requirement is that the photon energy has to be smaller than the work function. On the other hand $h\nu \geq E_{im} - E_F$ is necessary to populate the intermediate state by photon excitation.

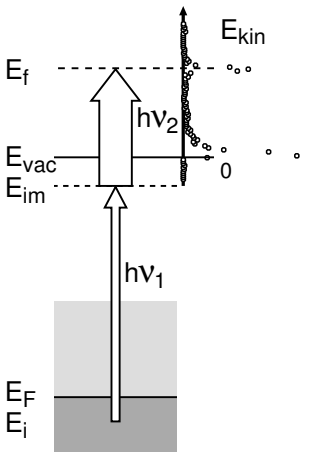

FIG. 2. Schematic energy diagram for the excitation steps in bichromatic two-photon photoemission. Spectra record the emitted electrons as a function of their kinetic energy.

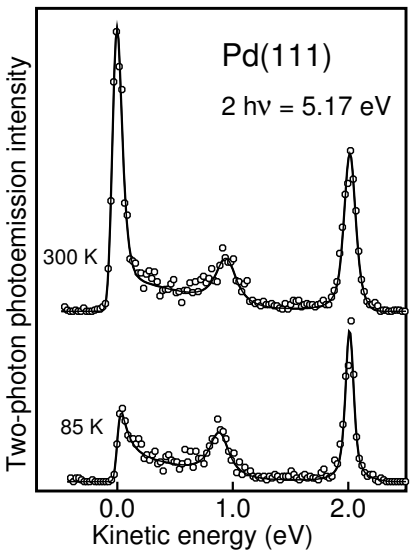

FIG. 3. Two-photon photoemission spectra from Pd(111) for 300 K and 85 K showing a strong decrease in the intensity of the low-energy peak originating from one-photon photoemission of thermally-excited electrons above E_F [*Fischer (1993)*].

Furthermore, the lifetime of the electron in the intermediate state must be sufficiently long to absorb a second photon. The quantitative meaning of this condition depends on the intensity of the photon beam. Because 2PPE is a second-order process, the signal increases quadratically with intensity. At constant photon flux the signal can be increased by better focusing, because it is inversely proportional to the size of the illuminated area. On the other hand, the intensity is limited by the heating of the sample and – even at much lower intensity – by severe space-charge effects. It has turned out in the past decade that image states on metal surfaces are sufficiently longlived to be investigated with the available pulsed lasers as light sources [*Giesen et al. (1985), Steinmann (1989)*]. That is the reason why we have chosen the study of image states as the most successful application of 2PPE spectroscopy.

The process shown in the right-hand scheme of Fig. 1 depicts the simplest case of monochromatic 2PPE: both photons have the same energy. The more general case, in which the energies are different, offers important advantages. In the monochromatic case, the signal S is proportional to the square of the intensity, $S \propto I^2(h\nu)$. In bichromatic 2PPE [*Schuppler et al. (1990a)*], $S \propto I(h\nu_1) \times I(h\nu_2)$. One can decrease $I(h\nu_1)$ and yet keep S constant by increasing $I(h\nu_2)$ accordingly. Figure 2 depicts a 2PPE process with $I(h\nu_2) \gg I(h\nu_1)$ as indicated by the width of the arrows. If, as in Fig. 2, E_{im} lies closely below E_{vac}, then $h\nu_1$ has to be close to the work function. In this case, one-photon photoemission of electrons excited thermally above E_F sets in, giving rise to a strong background signal. This leads to space-charge effects and, consequently, distorts the 2PPE spectrum. This can be avoided or at least reduced by decreasing $I(h\nu_1)$.

Bichromatic two-photon photoemission can be achieved without much additional effort in a straightforward way. The laser beam has to be frequency-doubled anyway in most cases to obtain UV photons $h\nu_1$; the fundamental (undoubled) beam can be used as $I(h\nu_2)$. This yields $h\nu_1 = 2 \times h\nu_2 = 2 \times h\nu$ and will be the situation considered in this chapter unless stated otherwise. The intensity condition $I(h\nu_2) \gg I(h\nu_1)$ is automatically fulfilled due to the limited efficiency of the frequency-doubling process. In time-resolved 2PPE [*Schoenlein et al. (1988)*] bichromatic measurements are mandatory in order to distinguish between the first and second step of the excitation.

2. Energy distribution curves

The results of two-photon photoemission are usually presented as energy distribution curves, much like in photoemission. The signal is the number of electrons as a function of the kinetic energy. A typical spectrum is indicated in Fig. 2. It exhibits two peaks, one at $E_{kin} = 0$ and another one at a higher energy $E_{kin} = E_f - E_{vac}$. The latter one is caused by excitation of the intermediate state E_i into the final state $E_f = E_{im} + h\nu_2$. The peak at $E_{kin} = 0$ is formed by one-photon photoemission of electrons excited thermally above E_F. This is apparent from the strong temperature dependence of the intensity of the low-energy peak shown in Fig. 3. The other two peaks seen in the spectra will be discussed in Sect. 2 1 3 (Fig. 7). The distribution can even quantitatively be accounted for by fitting the data points to a convolution

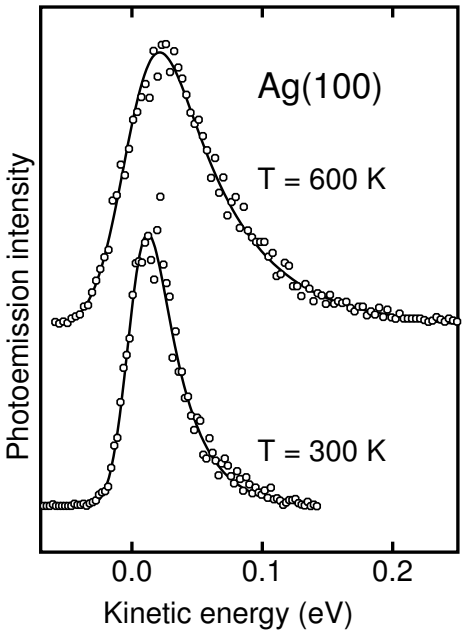

FIG. 4. Low-energy cutoff of two-photon photoemission spectra from Ag(100) for two temperatures and line fit of the tail of the Fermi distribution [*Schuppler et al. (1990a)*].

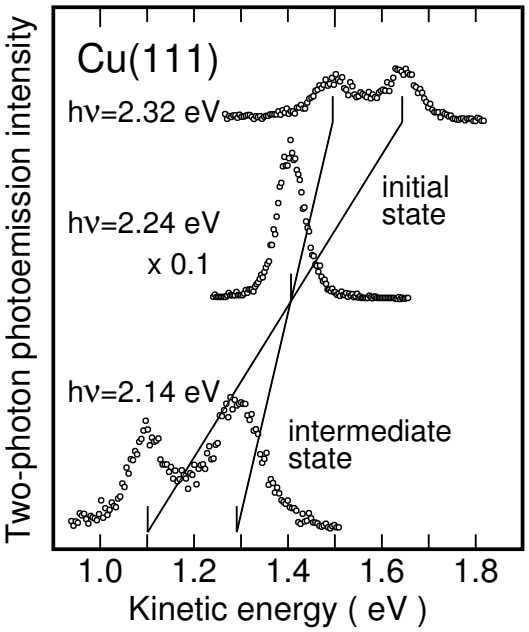

FIG. 5. Two-photon photoemission spectra from Cu(111) for different photon energies [*Wallauer*].

of the exponential tail of the Fermi distribution with a Gaussian representing the instrument function of the energy analyzer (see Fig. 4 and [*Schuppler et al. (1990a)*]).

The low-energy cutoff of the spectra corresponds to electrons leaving the sample with negligible kinetic energy and is related to the work function. If the work function changes in the course of an experiment, it will show up in a shift of the cutoff. This provides a sensitive way of monitoring the work function. For an absolute measurement of the work function Φ the high-energy cutoff $E_{kin}^{max} = h\nu_1 + h\nu_2 - \Phi$ formed by electrons excited from the Fermi level has to be determined (see Fig. 2). This is sometimes difficult in 2PPE because of missing intermediate states. Therefore, the work function is best measured in a one-photon photoemission spectrum.

The energy diagrams of Figs. 1 and 2 offer several possible reference levels. For the kinetic energy E_{kin} the vacuum level E_{vac} is the obvious choice and can be obtained directly from the spectrum by measuring the energy relative to the low-energy cutoff. When dealing with metal properties the Fermi energy is the appropriate reference level and $E_{im} - E_F = E_{kin} - h\nu_2 + \Phi$ is obtained. For image states (see Sect. 3) E_{vac} is the more convenient choice as reference energy. Positive binding energies E_b for bound states are obtained using the definition $E_b = E_{vac} - E_{im}$. The abscissa of the 2PPE spectra in this work are chosen appropriate to the physical interpretation. Data are always shown with increasing kinetic energy to the right, which yields increasing binding energies to the left.

3. Dependence on photon energy

In two-photon photoemission spectra both the height and the energetic position of a peak depend on the photon energy. If the initial state lies in a smooth continuum, as shown in Fig. 2, the intensity, i. e., the peak height should not change considerably with photon energy. If, however, E_i is an isolated, narrow state as indicated in Fig. 1, a pronounced resonance is expected at $h\nu = E_{im} - E_i$. The resonance curve, i. e., the peak height as a function of $h\nu$ has a width given by the width of both the initial and the intermediate state.

An example is two-photon photoemission from the Cu(111) surface. Three spectra, below, at, and above the resonance photon energy are shown in Fig. 5. The peak height is reduced by more than an order of magnitude $\sim$ 100 meV off resonance. The initial state responsible for this effect can be seen in the photoemission spectrum shown in Fig. 6. It is a surface state lying 0.39 eV below E_F. In addition to the drastic variation of the peak height, a splitting of the peak as well as an energy shift occurs off resonance (see Fig. 5). The splitting is due to the fact that both the initial and the intermediate state are visible off resonance. The energy shift may be deduced from Fig. 2. If the initial state E_i is kept constant while the photon energy is scanned, the kinetic energy will change three times as much: $\Delta E_{kin} = 3 \times \Delta h\nu$. If the intermediate state E_{im} is kept constant, the kinetic energy will change to the same extent as the photon energy: $\Delta E_{kin} = \Delta h\nu$. In Fig. 5 the smaller peak in the bottom curve and the higher peak in the top curve rep-

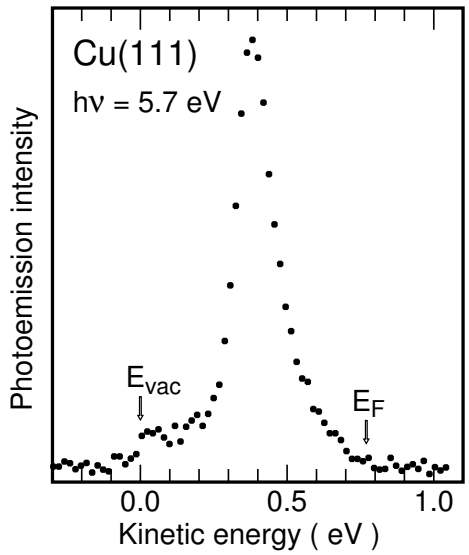

FIG. 6. Photoemission spectrum from Cu(111) taken at 5.7 eV photon energy with the monochromatized radiation from a deuterium lamp [*Wallauer*].

resent the initial state appearing in the photoemission spectrum in Fig. 6. The higher peak in the bottom curve and the smaller peak in the top curve correspond to the intermediate state.

So far, we have assumed that the intermediate state lies closer to the vacuum level than to the Fermi level: $E_{im} - E_F > \Phi/2$. If this condition does not hold, the order of excitation in bichromatic 2PPE is reversed: The intermediate state is populated by $h\nu$ (or $2h\nu$) and ionized by $2h\nu$. In 2PPE from the Pd(111) surface both cases are realized (see Fig. 7). The spectrum exhibits two peaks (see Fig. 3), corresponding to the two intermediate states. The kinetic energy of the lower peak, caused by the surface state as intermediate state changes as $\Delta E_{kin} = 2 \times \Delta h\nu$, because E_{im} is constant and $E_{im} - E_F < \Phi/2$.

The shift in peak energy upon variation of the photon energy, therefore, allows one to identify a peak in a 2PPE spectrum as being due to an initial state, an intermediate state close to the Fermi level, or an intermediate state close to the vacuum level.

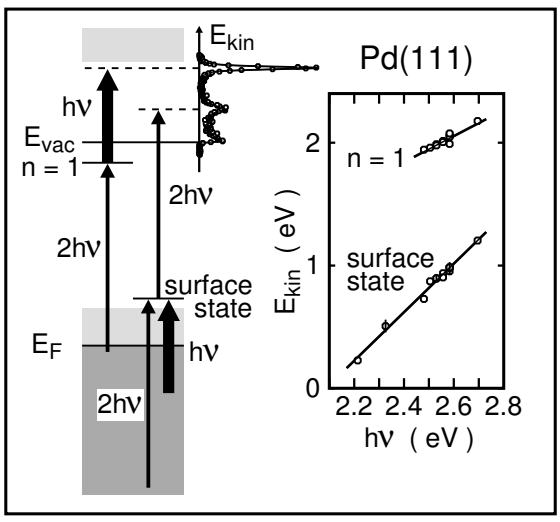

FIG. 7. Excitation scheme of bichromatic two-photon photoemission at a Pd(111) surface [*Fischer et al. (1993c)*]. The $n = 1$ state (4.89 eV above E_F) is ionized by a photon of energy $h\nu$. The surface state (1.26 eV above E_F) is ionized by a photon of energy $2h\nu$. These states show (inset) a different dependence of the kinetic energy with photon energy.

4. Dependence on angle of emission

Two-photon photoemission spectra generally change with the angle of emission. Hence, good angular resolution is required for well-defined conditions. The spectra presented in this chapter have usually been taken at normal emission with an acceptance angle of a few degrees or less. As the electronic states involved are surface states, they are located in the center of the surface Brillouin zone. If a bulk state has to be considered, it lies on the line of the Brillouin zone corresponding to the

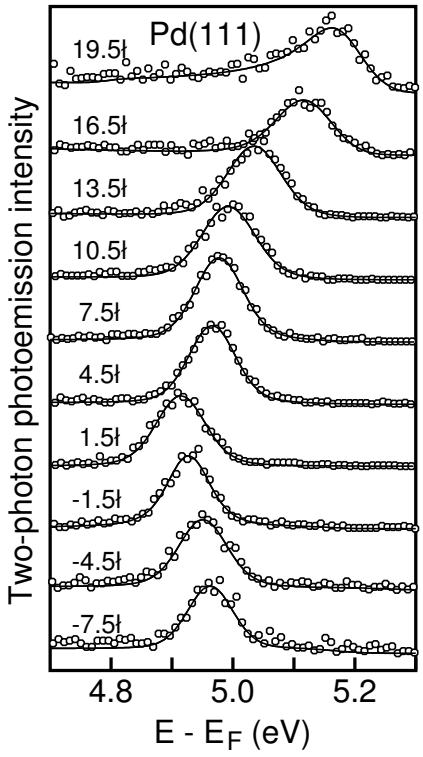

FIG. 8. Two-photon photoemission spectra of the lowest image states on Pd(111) for different emission angles ($2h\nu = 5.17$ eV) [*Fischer (1993)*].

surface orientation. The component of the k vector parallel to the surface is obtained from the emission angle θ by $\hbar k_{\parallel} = \sqrt{2mE_{kin}}\sin\theta$. It is conserved in the emission process [*Kevan (1992)*]

Consequently, by measuring the angle dependence of the peak position $E_f(\theta)$ the dispersion $E_{im}(k_{\parallel})$ or $E_i(k_{\parallel})$ can be determined. An example for the angle dependence of the peak position is shown in Fig. 8 for the intermediate state labeled $n = 1$ in Fig. 7.

5. Linewidth and lifetime

The width of a peak in a two-photon photoemission spectrum is an indication of the lifetime of the corresponding state, provided the peak does not consist of several unresolved lines and the resolution of the energy analyzer is good enough. This has been widely used in 2PPE spectroscopy for determining the lifetime of intermediate states. If the analyzer function has a width which is small compared to the width of the Lorentzian representing the lifetime-broadened line profile of the state, then the measured linewidth Γ is related to the lifetime τ by $\Gamma \cdot \tau = \hbar = 660$ meV·fs.

If the width of the analyzer function is comparable to the intrinsic linewidth, the lifetime may still be determined by line-profile analysis, fitting the experimental data points with a convolution of the analyzer function and a Lorentzian of adjustable width [*Schuppler et al. (1990a), Fischer et al. (1990)*]. The width of the analyzer function, which is well approximated by a Gaussian, can be determined by fitting the low-energy cutoff (see Fig. 4) or from the width of a line with an intrinsic width which is so small that the measured width is equal to the one of the analyzer function.

The linewidth should not be measured in spectra taken with resonant photon energy, because in resonance the line tends to be narrower than off resonance [*Merry et al. (1993), Reuß (1994)*]. This is due to the width of the initial state: The resulting line profile is the product of the line profiles of the initial and the intermediate state. If off-resonance spectra are not available with a quality sufficient for line-profile analysis, a profile measured in resonance has to be corrected for this effect.

An alternative way of measuring the lifetime of an intermediate state is time-resolved spectroscopy [*Schoenlein et al. (1988), Schoenlein et al. (1990), Schoenlein et al. (1991)*]. The probe pulse $h\nu$ which ionizes the intermediate state is delayed with respect to the pump pulse $2h\nu$ which populates it (see Fig. 2). The decrease of the signal with increasing delay time is a direct measure of the lifetime. The method is limited by the available laser-pulse length: The lifetime cannot be much shorter than the pulse length.

Line-profile analysis and time-resolved spectroscopy are complementary methods of measuring the lifetime. Short lifetimes with correspondingly broad lines are best determined by measuring the width. The longer the lifetime the more feasible and accurate becomes time-resolved spectroscopy. Most of the results on lifetimes reported in this chapter have been obtained by line-profile analysis with an analyzer function of up to 27 meV width corresponding to 24 fs. The results of time-resolved spectroscopy have been obtained with laser pulses of 55 fs length corresponding to 12 meV. There is a range of the intrinsic width from 12 to 27 meV corresponding to lifetimes between 24 an 55 fs where both methods have to be stressed to their limits leading to larger experimental errors. Recently, the resolution of the energy analysis has been improved to 5 meV [*Padowitz et al. (1992)*], which corresponds to 132 fs. This closes the gap and leads to a considerable overlap of the two methods.

2. Experimental arrangements

The experimental requirements for two-photon photoemission are the same as for photoemission with the exception of the light source. The high intensity needed for 2PPE can only be provided by a pulsed laser. The experimental arrangement, shown schematically in Fig. 9, consequently consists of a laser system as light source, and a UHV sample chamber, containing equipment for surface preparation and analysis and an electron energy analyzer; in addition, a low-pressure gas-discharge lamp is connected to the sample chamber for one-photon photoelectron spectroscopy. This experimental arrangement [*Giesen (1986), Hage (1986), Schuppler (1991)*] has been used to obtain most data presented in this chapter. Other setups have been described [*Kubiak (1987), Kubiak (1988), Nielsen et al. (1989), Wu et al. (1992), Padowitz et al. (1992), Merry et al. (1993), Lingle et al. (1993)*] and will be mentioned in the appropriate section if the difference is important in the present context. The equipment for time-resolved spectroscopy is described in Sect. 2 2 4.

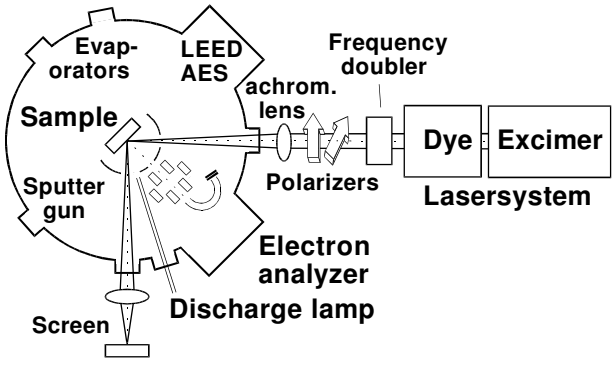

FIG. 9. Schematic setup of a two-photon photoemission experiment.

1. Light source

The light source is a three-stage dye laser pumped by a XeCl excimer laser which emits 20 ns pulses with a pulse energy of up to 150 mJ at a repetition rate of 50 Hz. With a set of suitable dyes the laser can be tuned to any photon energy in the range 1.7 eV to 3.4 eV with a pulse energy of ≤ 15 mJ. Frequency doubling in KDP (KH_2PO_4) and BBO (BaB_2O_4) covers the range up to 5.63 eV. This is sufficient for most surfaces because $2h\nu < \Phi$ is obligatory to avoid one-photon photoemission. After frequency doubling the pulse energy is ≤ 1.5 mJ.

In bichromatic two-photon photoemission both the fundamental wave and the second harmonic are used. They are perpendicularly polarized. The intensity ratio can be varied with a polarizer. A second polarizer is used to define the polarization of the light incident onto the sample. The polarization vector has to be parallel to the plane of incidence (see Fig. 9) for 2PPE experiments on image states.

The light is focused onto the sample by an achromatic UV lens. Fused quartz windows are used to seal off the vacuum chamber. The pulse energy reaching the surface is typically ≤ 0.15 mJ in an area of ≤ 1 mm^2. The light spot can be observed in the enlarged image projected onto the screen by the reflected light.

Only a fraction of the available intensity can be used. The usable UV intensity is limited to < 300 kW/cm^2 by space-charge effects which shift and broaden the measured energy distribution [*Giesen et al. (1985), Kubiak (1987)*]. The space charge is built up by the low-energy electrons which arise mainly from one-photon photoemission [induced by the UV light] of thermally excited electrons in states above E_F (see Sect. 2 1 2). The space charge can be reduced in the bichromatic mode (see Sect. 2 1 1 and [*Schuppler et al. (1990a)*]) and for photon energies not too close to the work function [$(\Phi - 2h\nu) \gg kT$]. Alternatively, the pulse length can be reduced to the limit of less than one electron emitted per pulse. By an increase of the repetition rate of the laser the overall count rate may actually be increased [*Padowitz et al. (1992), Merry et al. (1993)*]. Energy- and angle-integrated 2PPE signals correspond typically to 10^{12} electrons per second emitted during the pulse [*Strupp et al. (1993)*]. This number shows that space charge poses no problems for lasers with a pulse length in the ps or fs regime [*Padowitz et al. (1992), Schoenlein et al. (1988), Schoenlein et al. (1990), Schoenlein et al. (1991)*].

2. Sample chamber

The surface sensitivity of two-photon photoemission and the reactivity of some of the surfaces makes it necessary to keep the pressure in the sample chamber in the 10^{-11} mbar range in order to keep the surface clean during the measurement. This pressure can be maintained as long as the discharge lamp is closed off by a valve. During the evaporation of metals the pressure may rise to the low 10^{-10} mbar range.

By moving the sample perpendicular to the optical plane of incidence it can be positioned in two planes: the measurement plane contains the light sources, the windows for the incident and reflected light, and the electron energy analyzer. The preparation plane contains an ion gun, an electron gun with LEED optics for investigating the surface structure by low-energy electron diffraction and for Auger electron spectroscopy, and the evaporation sources.

3. Electron energy analyzer

A hemispherical (160°) electrostatic analyzer is used to measure the energy distribution of the photoelectrons. It is equipped with electron optics consisting of three immersion lenses each, at the entrance and exit side. This improves the transparency of the analyzer and suppresses secondary electrons. The analyzer is shielded against magnetic fields with a double μ-metal case. The energy resolution has been experimentally determined [*Schuppler (1991)*] from the low-energy cutoff of photoemission spectra to $\Delta E/E_{pass} = 0.027$ for $E_{pass} \geq 1$ eV. For high resolution, the pass energy is chosen to be 1 eV. In most cases, resolution is traded in for intensity by increasing the pass energy to typically 1.6 eV.

The angle of emission can be varied by rotating the sample around an axis perpendicular to the measurement plane. The angular resolution of the analyzer combined with the electron optics is calculated to be 0.6°. Experimental tests have shown that this is actually achieved [*Schuppler (1991)*]. For a kinetic energy of 2 eV (typical for image-state electrons in bichromatic 2PPE) this corresponds to a resolution of the k vector parallel to the surface $\Delta k_{\|} = 0.007$ Å^{-1}.

The maximum signal measured behind the exit slit is less than one electron per laser pulse corresponding to a count rate of 50 electrons per second with a laser repetition rate of 50 Hz. The rare event that more than one electron per pulse arrives at the detector is taken care by pulse-height analysis.

An alternative way of measuring the energy distribution is time-of-flight analysis [*Padowitz et al. (1992), Merry et al. (1993)*]. For 2PPE spectroscopy it is particularly appropriate in view of the short laser pulses. Obviously, best results are to be expected with the ps-pulses of the high-frequency laser. In this case, even with a relatively short flight tube (13.5 cm), the resolution could be improved by a factor of five. With a delayed-coincidence method an instrument function of 100 ps FWHM could be achieved, which results in an energy resolution of 5

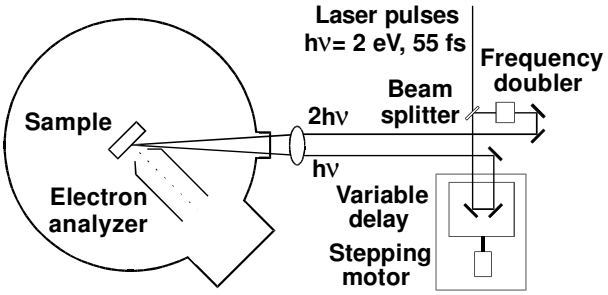

FIG. 10. Schematic setup of a time-resolved two-photon photoemission experiment.

meV. At an acceptance angle of ±1.5° a 2PPE signal of 0.01 electron per pulse was recorded. The repetition rate of 2 MHz leads to count rates of several kHz.

For an absolute determination of the kinetic energy, the difference in work function between the sample and the detector has to be compensated by the proper bias voltage. This limits the accuracy of the energy data. The limit of error is in the 10 – 50 meV range. Better accuracy can be achieved if a series of peaks converging towards the vacuum level is observed.

4. Time-resolved spectroscopy

Time-resolved two-photon photoemission spectroscopy was developed and applied to lifetime measurements by Schoenlein, Fujimoto, Eesley, and Capehart [*Schoenlein et al. (1988), Schoenlein et al. (1990), Schoenlein et al. (1991)*]. The experimental arrangement is shown schematically in Fig. 10. A mode-locked ring dye laser and a copper-vapor laser amplifier delivers pulses with a width of 55 fs at a repetition rate of 8 kHz; the pulse energy is 2 μJ and the photon energy is 2 eV. The beamsplitter divides the pulse into pump and probe. The probe pulse is delayed with respect to the pump pulse by the translational stage which is controlled by the stepping motor with 0.1 μm steps. The photon energy of the pump pulse is doubled by a KDP crystal. Care has to be taken to avoid pulse broadening. Pump and probe pulse are combined in a collinear geometry and focused by a curved Aluminum mirror (not shown in Fig. 10). The spot size on the sample surface is 20 μm. This leads to an energy density of 60 μJ/cm^2 for the pump pulse and 700 μJ/cm^2 for probe pulse, comparable to the situation in ordinary 2PPE spectroscopy. A cylindrical-mirror analyzer is used as electron spectrometer. The energy resolution is 180 meV with a pass energy of 10 eV; the angular resolution is 10°. The peak signal is $7.5 \cdot 10^{-2}$ electrons per pulse; with the repetition rate of 8 kHz, this results in a counting rate of 600 counts per second.

With this arrangement the lifetime of intermediate states with $E_{im} - E_F \leq 4$ eV can be measured. For studying states lying further away from the Fermi energy, the 2 eV pulse in the pump arm behind the beamsplitter is amplified and focused in a jet of ethylene glycol. This produces a spectral continuum a suitable portion of which is sent through the frequency doubler. In this way 80 fs pulses with a photon energy of 4.35 eV as well as 90 fs pulses with 4.41 eV photons could be created.

3. IMAGE STATES

1. General concept

An electron placed at a distance z in front of a metal surface induces an electric field. This field leads to a rearrangement of the charge in the metal in such a way that the parallel component of the field vanishes at the surface of the conductor. The electron and an opposite charge placed at $-z$ (Fig. 11 top) produce in vacuum an electric field which is perpendicular to the surface in the whole surface plane. This describes the field outside the surface correctly. The field inside the metal is due to a suitable rearrangement of the metal electrons which produces a field satisfying the appropriate boundary conditions at the surface. If the electron comes closer to the

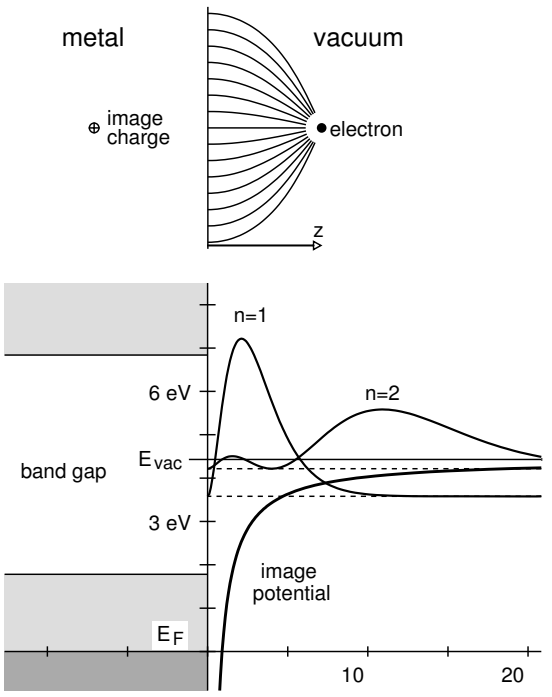

FIG. 11. Top: The electric field of an electron in front of a metal surface can be described by the concept of an image charge. Bottom: The corresponding attractive image potential leads to a series of bound states if the electron cannot penetrate into the metal along certain directions due to a band gap. For the lowest two states, the square of the wave function is shown.

surface, the charge rearrangement changes such that the hypothetical opposite charge moves like an image of the electron towards the surface. This concept leads to an attractive image force

$$F(z) = -\frac{e^2}{4\pi\epsilon_0}\frac{1}{(2z)^2} \tag{1}$$

acting on the electron in front of a metal surface. It can be derived from a Coulomb-like potential approaching the vacuum energy E_{vac} for large distances:

$$V(z) = E_{vac} - \frac{e^2}{4\pi\epsilon_0}\frac{1}{4z}\ . \tag{2}$$

The factor 4 in the denominator of this image potential arises because the electron and the image charge are separated by a distance $2z$. The electron may not be able to penetrate into the metal along certain directions due to band-structure effects. If its energy is below E_{vac} it cannot overcome the vacuum barrier and becomes trapped in front of the surface. The situation corresponds to the Coulomb problem in one dimension and the quantum-mechanical solution is analogous to the hydrogen atom. The resulting image states form a series of bound states (numbered by n) converging towards E_{vac} with energies [*Echenique and Pendry (1978)*]

$$E(n) = E_{vac} - 0.85\ \mathrm{eV}/n^2\ ,\ n = 1, 2, \ldots \tag{3}$$

The potential reduced by a factor 4 compared to the hydrogen atom leads to binding energies of the states which are smaller by a factor of 16. The wave functions are obtained from the radial part of the wave function for the hydrogen atom multiplied by z (due to the changed dimension) and expanded by a factor of 4 (due to the weaker potential) [*Straub and Himpsel (1986), Echenique and Pendry (1990)*]. The maximum of the wave function for the $n = 1(2)$ state is more than 2 (10) Å away from the surface (see Fig. 11 bottom).

2. Calculation of surface states

The concept of image states outlined in the preceding section has to be improved for a correct description of the experimental findings. The divergent image potential has to be joined smoothly to the potential of the metal at the surface. The neglect of the penetration of the wave function into the metal is removed by the use of the complex band structure for the proper description of bulk band gaps. Because of the small corrugation of the potential in the region of the image states and by the use of a suitable effective bulk potential, the one-dimensional picture for the calculation of image states can be retained. It is convenient to calculate the wave function in the Coulomb-like potential outside the surface and in the periodic bulk potential independently.

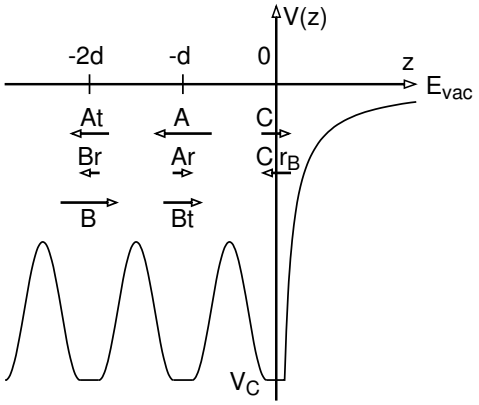

FIG. 12. Schematic potential for a one-dimensional solid near the surface [*Fauster (1994)*]. The wave function between the atomic layers is described by a superposition of waves of amplitude A and B traveling to the left and right, respectively. The fraction t is transmitted and the fraction r is reflected. At the surface ($z = 0$) the bulk wave function is matched to the wave of amplitude C reflected (coefficient r_B) by the vacuum barrier.

Both solutions have to go to zero for large distances away from the surface. Image states are obtained for energies at which the two solutions and their derivatives can be joined continuously at the surface.

1. Wave function outside the surface

The potential Eq. 2 is asymptotically exact for large distances away from the surfaces. Corrections are needed only close to the surface, because the charge density of the solid decays exponentially into the vacuum. The position of the maximum of the wave function of the first image state is more than 2 Å away from the surface (see Fig. 11). At this distance the charge density is already rather small, so the corrections to the potential can be neglected in first approximation. The simplest way to achieve a continuous potential is to join it continuously to the bulk potential as illustrated in Fig. 12. The remaining degree of freedom in the choice of the potential is the position of the $z = 0$ surface with respect to the outermost atomic layer. In this work the image plane is chosen at one half of a layer distance outside the last layer of atoms, avoiding the introduction of an additional parameter. By an adjustment of the image-plane position better agreement between calculation and experiment can be obtained [*Smith and Chen (1991)*]. Various other forms of the potential near the surface have been proposed which require the numerical integration of the Schrödinger equation to obtain the binding energies and the wave function [*Jones et al. (1984), Borstel and Thörner (1988), Smith et al. (1989), Graß et al. (1993)*].

The knowledge of the complete solutions in the bulk

and on the vacuum side is not needed for the wave-function matching at the surface, if one is interested only in the binding energies of the image states. The wave function and its derivative at the surface can be obtained in a one-dimensional scattering approach [*Echenique and Pendry (1978)*]. The wave of amplitude C is reflected by the vacuum barrier with a reflection amplitude r_B (see Fig. 12). If the electron energy is below E_{vac} the transmission probability is zero and the reflection coefficient can be written as $r_B = \exp(i\phi_B)$. For the wave function at the surface the plane-wave expansion is

$$\varphi(z) = Ce^{iKz} + Ce^{i\phi_B}e^{-iKz} \ , \tag{4}$$

which is valid only in an infinitesimal range around $z = 0$. In this region the potential is assumed to have the constant value V_C and the wave vector K is given by $E - V_C = \hbar^2K^2/2m$. The behavior of the wave function at the surface is given by the barrier phase ϕ_B. Its energy dependence can be approximated for the potential Eq. 2 by the following expression [*McRae (1979)*]

$$\phi_B(E) = \pi(\sqrt{(3.4 \text{ eV})/(E_{vac} - E)} - 1) \ . \tag{5}$$

The wave function and its derivative can be easily evaluated as a function of energy with Eqs. 4 and 5.

2. Complex band structure

The band structure $E(k)$ of solids permits only certain energies E as a function of the wave vector k. The introduction of a surface changes the boundary conditions and permits complex values of k which describe waves decaying exponentially into the bulk. The resulting band structure becomes complex and can be easily calculated in the two-band approximation to the nearly-free-electron model [*Smith (1985)*]. An alternate one-dimensional model for the complex band structure can be obtained with a scattering approach [*Ashcroft and Mermin (1976)*]. As sketched in Fig. 12, the solid is composed of individual layers with a (possibly infinitesimal) region between the layers with a constant potential V_C. In this region the wave function can be expanded into plane waves

$$\psi(z) = Ae^{-iKz} + Are^{iKz} + Bte^{iKz} \ . \tag{6}$$

The transmission and reflection coefficients are connected by the requirement of continuity $|t|^2 + |r|^2 = 1$. In the cases considered here the following choices are made: $t = |t|$ real and $r = \sqrt{t^2 - 1}$ purely imaginary [*Pendry (1974)*]. This avoids the introduction of an additional parameter for the complex phase of t [*Ashcroft and Mermin (1976)*]. The wave vector K is given by the energy E relative to the potential V_C by $E - V_C = \hbar^2K^2/2m$,

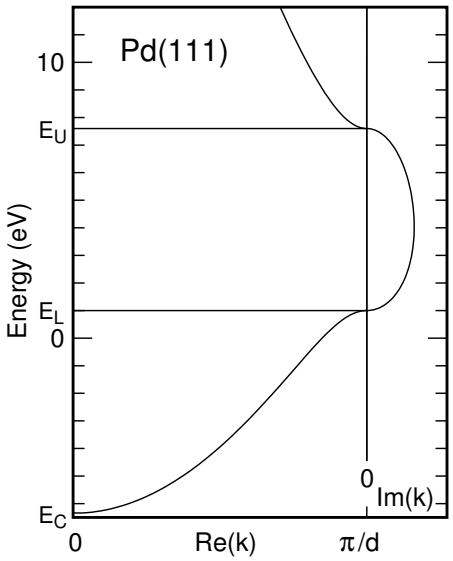

FIG. 13. Complex band structure obtained with the one-dimensional scattering model using a constant real transmission coefficient t [*Fauster (1994)*]. The parameters have been adjusted to match the bottom of the valence band E_C and the lower (E_L) and upper (E_U) band edges for Pd(111). The energy scale is relative to the Fermi level.

where m denotes the (effective) mass of the electron. According to Bloch's theorem the solutions in the periodic potential with period d must obey

$$\psi(z + d) = e^{ikd}\psi(z) \tag{7}$$

for all z and in particular between the layers and at $z = -2d$. The solutions for the wave vector k can be found by inserting Eq. 6 and the analogous expansion at $z = -2d$ from Fig. 12 into Eq. 7 and applying the same procedure to the derivatives of the wave function. This yields the following equation [*Ashcroft and Mermin (1976)*]

$$\cos(Kd) = t\cos(kd) \ . \tag{8}$$

Real solutions for the wave vector k are obtained for $|\cos(Kd)| < t$ and describe propagating Bloch waves. Wave vectors with a non-vanishing imaginary part indicate exponentially decaying or increasing solutions in band gaps. Because solutions of Eq. 8 come in pairs k and $-k$, a wave function decaying into the bulk can be always found at a given energy in the band gap. For the ratio of the amplitudes in Eq. 6, the two solutions at a given energy are given by

$$(A/B)_k = (e^{ikd}/e^{iKd} - t)/r = (B/A)_{-k} \ . \tag{9}$$

The edges of the band gaps are given by the condition $|\cos(kd)| = 1$. For low energies, the relevant parameters of the band structure are the lower and upper band edges, E_L and E_U, and the bottom of the valence band E_C

	E_C	E_L	E_U	t
Ag(100)	−7.8	1.78	6.84	0.947
Ag(111)	−7.8	−0.31	3.99	0.939
Au(111)	−9.0	−1.00	3.60	0.939
Cu(100)	−8.6	1.80	7.9	0.937
Cu(111)	−8.6	−0.85	4.1	0.929
Pd(111)	−6.35	1.0	7.6	0.884
Ni(100)	−8.8	2.53	9.33	0.935
Ni(111)	−8.8	−0.9	6.5	0.877
Co(0001)	−8.7	−1.15	6.4	0.866
Fe(110)	−8.0	0.48	7.88	0.900

TABLE 1. Band-structure parameters in eV relative to E_F from [*Echenique and Pendry (1990), Himpsel (1991), Fauster (1994)*]. From the energies at the bottom of the valence band E_C and the lower and upper edge E_L and E_U of the band gap the transmission coefficient t of the one-dimensional scattering model can be calculated with Eqs. 10 and 11.

(see Fig. 13). The solutions of $|\cos(Kd)| = t$ at the gap edges and the bottom of the band give a system of three equations [*Fauster (1994)*]. It can be solved for an energy-independent transmission coefficient

$$t = \cos(\pi(E_U - E_L)/4E_g) \tag{10}$$

and the factor E_g containing the effective mass m

$$E_g = \hbar^2\pi^2/2md^2 = (E_U - E_C + E_L - E_C)/2 \; . \tag{11}$$

This is just the energy of the center of the band gap relative to the bottom of the band E_C. The constant reference potential is slightly below E_C,

$$V_C = E_C - (E_U - E_L)^2/16E_g \; . \tag{12}$$

These equations show that the transmission coefficient is just a measure for the ratio of the gap width to the mid-gap energy. Table 1 lists the band-structure parameters for the surfaces discussed in this work which yield transmission coefficients between 0.866 and 0.947. The complex band structure of Eq. 8 calculated for Pd(111) with the parameters obtained from Eqs. 10 through 12 is shown in Fig. 13. The result is almost identical to the solution of the well-known two-band model [*Fauster (1994)*].

3. Wave-function matching at the surface

Equations 6 and 4 at $z = 0$ give as a necessary condition for the continuity of the wave function and its derivative at the surface a set of two homogeneous linear equations for the amplitudes A and C. Nontrivial solutions are obtained only for certain energies where the determinant vanishes. One of the advantages of the method is that the coefficients entering the equations can be easily calculated as a function of energy with the use of Eqs. 8, 9, and 5.

Instead of searching for the zeros of the determinant of the linear equation it is more convenient to find the maxima in the reciprocal value of the determinant as a function of energy. This procedure works also for energies outside the band gap and for a non-vanishing imaginary part of the potential V_C which can be introduced without problems into the complex equations of Sect. 3 2 2. In practical applications it is convenient to include always a small imaginary part of V_C to avoid numerical complications. It can by chosen sufficiently small ($< 10^{-3}$ eV) if results for a real potential V_C are wanted. The imaginary part of the potential allows for the finite lifetime and penetration of the excited states in particular at energies outside the band gap.

4. Extension to overlayers and alloys

The one-dimensional scattering model can easily be extended to include the effects of additional overlayers on the surface. At the interface the wave function of the substrate has to be matched to the solution for the overlayer. The latter is given by a linear combination of both solutions of Eq. 8, because the condition that the wave function decays into the solid does not hold in the overlayer. The matching conditions can be obtained by evaluating Eq. 6 at the left side of the overlayer ($z = -d$) using Eq. 9 and different amplitudes A_1 and A_2 for the two solutions. The resulting set of linear equations is easily solved and with the help of Bloch's theorem Eq. 7 the wave function and its derivative can be evaluated at the surface of the overlayer. This information is sufficient to add another overlayer or to determine the energy of surface states as described in Section 3 2.

It should be emphasized that the one-dimensional scattering approach describes the behavior of the overlayer based on the band structure of the bulk material and introduces no additional parameters. The proper convergence behavior for thick layers is obtained. The properties of the individual layers are derived in a physically meaningful way by the transmission coefficient t.

The one-dimensional scattering approach can be extended also to the case of an alloy surface. The transmission coefficient of a layer can be regarded as the effective sum of the scattering by all ion cores of the atoms in the layer. For an alloy consisting of elements X and Y, the transmission coefficient is the result of a suitable average over all atoms in the layer. If the relative concentrations of the constituents are x and $y = 1 - x$ a reasonable assumption for the transmission coefficient of the alloy layer is

$$t(x) = x\, t_{\mathrm{X}} + (1 - x)\, t_{\mathrm{Y}} \; . \tag{13}$$

Similar equations are used for the parameters V_C and E_g. This ansatz ensures the proper behavior in the limiting cases $x = 0$ and $x = 1$. It is obvious that for the one-dimensional case the layer structure has to be retained in the alloy. It should be emphasized that within the scattering model the properties of an alloy of given concentration are determined completely by the band-structure parameters of the constituents.

The combination of the extensions to the one-dimensional scattering model to overlayers and alloys yields the solution to the otherwise almost intractable problem of a surface with a concentration gradient. Such a situation can occur for segregation at an alloy surface or for an intermixed interface of an overlayer system. Starting from the bulk (of constant concentration) individual layers are added until the surface is reached. The transmission of each layer is calculated using Eq. 13 with the appropriate concentration.

3. Phase analysis model

Section 3 2 3 showed that the matching condition at the surface determines the energies of the image states. This is supported by the experimental data in Sect. 4 1. The picture of the reflection of the electron wave by the surface barrier in Fig. 12 can be extended to the bulk side. The reflection at the crystal adds a phase shift ϕ_C in a plane-wave expansion analogous to Eq. 4. Stationary states are obtained if the total phase shift $\phi_B + \phi_C$ adds up to a multiple of 2π [*Echenique and Pendry (1978)*]. The crystal phase shift ϕ_C can be calculated from the solution of the one-dimensional scattering model or within the two-band approximation [*Smith (1985)*]. The image-states series covers an energy range of less than 0.85 eV, where the crystal phase can be considered to be constant in good approximation. The condition

$$\phi_B + \phi_C = 2\pi n \tag{14}$$

leads then in combination with Eq. 5 to the following expression for the energies of the image states

$$E(n) = E_{vac} - 0.85 \text{ eV}/(n+a)^2 \ , \ n = 1, 2, \ldots \tag{15}$$

This is identical to Eq. 3 except for the the quantum defect a which is related to the phase ϕ_C of the wave function at the surface [*Echenique and Pendry (1978)*]

$$a = (1 - \phi_C/\pi)/2 \ . \tag{16}$$

The crystal phase shift ϕ_C varies continuously from 0 to π going from the bottom to the top of the band gap [*Smith (1985)*]. The quantum defect a is 0 at the top of the band gap and reaches its maximum value of 1/2 at the bottom.

The quantum-defect formula Eq. 15 can be used to determine the work function in an independent way from the convergence behavior of the image-state series. The experiment measures the kinetic energies relative to the vacuum energy of the analyzer which is equivalent to the Fermi energy at fixed analyzer work function. Consequently, the image states are obtained in the experiment relative to the Fermi energy. The determination of the sample work function requires the knowledge of the low-energy cutoff. If two or more image-state energies are known relative to E_F, their energy separation can be used to determine the quantum defect a in Eq. 15. Because the image-state energies are known relative to E_F, one obtains the work function $\Phi = E_{vac} - E_F$ from Eq. 15. The extrapolated work function agrees for clean surfaces within the experimental errors with the measured work function. For inhomogeneous surfaces the extrapolation of the work function from the image-state series using the quantum-defect model plays an important role as will be demonstrated in Sect. 5.

4. IMAGE STATES ON CLEAN SURFACES

Image states at metal surfaces have first been detected and identified experimentally by inverse photoemission [*Johnson and Smith (1983), Dose et al. (1984), Straub and Himpsel (1984), Straub and Himpsel (1986)*]. The first high-resolution measurements of image states with 2PPE spectroscopy [*Giesen et al. (1985)*] were made on Ag(111) and Cu(111) surfaces, where a narrow surface state lies just below the Fermi level (see Fig. 15) which can be used as initial state to populate the image state

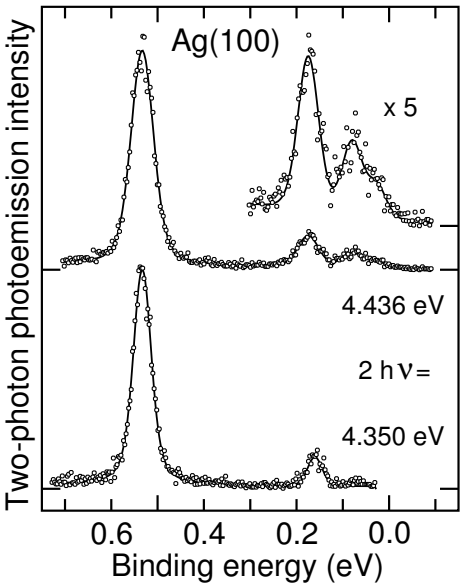

FIG. 14. Two-photon photoemission spectra from Ag(100) measured at two different photon energies [*Schuppler et al. (1990a)*]. The enlarged portion of the upper spectrum shows the $n = 4$ state as a shoulder.

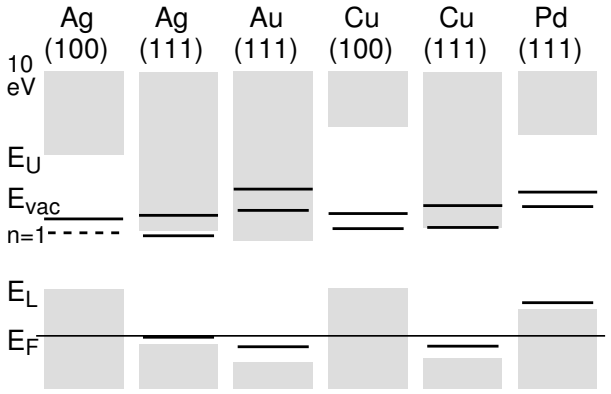

FIG. 15. Band structure for the surfaces shown in Fig. 16. The projected bulk bands along the surface normal are indicated by the shaded areas. The vacuum level is shown by solid lines slightly above the $n = 1$ image state (dashed lines). Dashed lines near the bottom of the band gaps indicate surface states.

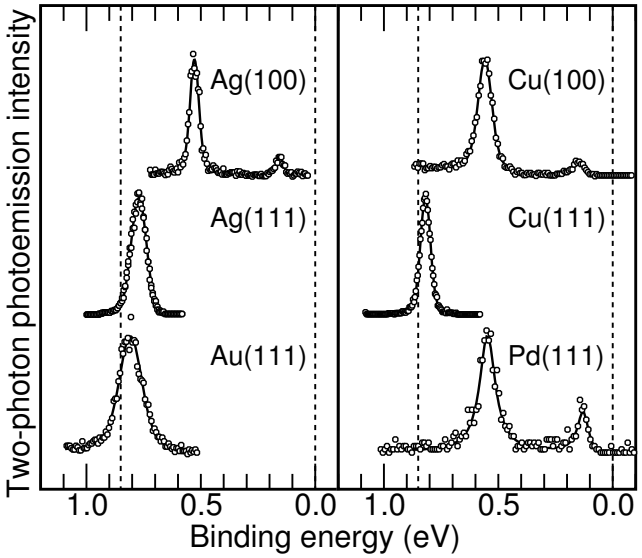

FIG. 16. Two-photon photoemission spectra for various surfaces.

in resonance (see Sect. 2 1 3); this facilitates the detection in 2PPE. For the (100) surfaces of Ag and Cu the Fermi level lies below the bottom of the gap (see Fig. 15 and Tab. 1). Consequently, there is no surface state below E_F and the image state has to be populated from the continuum of the bulk states. This reduces the 2PPE signal by more than an order of magnitude, because there is no resonance and the overlap with the wave function of the image state is not as good for bulk states. Nevertheless up to four members of the Rydberg series (see Eq. 15) could be identified. The spectrum for Ag(100) is shown in Fig. 14 as one of the best examples [*Schuppler et al. (1990a)*]. The line is the fit obtained by the sum of four Lorentzians convoluted with a Gaussian (see Sect. 2 1 5). In this way the binding energy and the width can be determined for each peak.

1. Binding energies

Two-photon photoemission spectra of noble metal surfaces are presented in Fig. 16. The binding energy of 0.85 eV from the simple hydrogen model Eq. 3 is indicated by a dashed line. Image states on the (111) surfaces of Ag [*Giesen et al. (1985)*], Au [*Reuß (1994)*], and Cu [*Giesen et al. (1986), Schuppler et al. (1992)*] have binding energies close to this value which means that the quantum defect is small, $\phi_C \approx \pi$ (see Eq. 15). This holds at the top of the gap. As can be seen in Fig. 15 the image states on these surfaces lie closely below, at, or even above E_U. Obviously the position of the vacuum energy relative to the gap is decisive for the binding energy. For Ag(100) [*Giesen et al. (1987a), Schuppler et al. (1990a)*], Cu(100) [*Giesen et al. (1987a)*], and Pd(111) [*Fischer et al. (1993c)*] binding energies between 0.5 and 0.6 eV are found. The quantum defect is 0.2 to 0.3 in these cases. Consequently, the image state has to lie close to the middle of the gap, which is in fact characteristic for these surfaces (see Fig. 15).

The reason for this dependence of the binding energy on the position of the image state relative to the gap is the requirement to match the wave functions at the surfaces. This is demonstrated in Fig. 17. The image state on Cu(111) [*Giesen et al. (1986), Schuppler et al. (1992)*] is located right at the top of the gap ($E_{im} - E_U \approx 0$). Both the hydrogen-like wave function in the region of the image potential and the s-like wave function in the bulk have nodes at the surface. They are matched by adjusting the amplitudes such that the derivative is equal on both sides of the surface. The resulting binding energy of 0.83 eV is very close to the hydrogenic value of 0.85 eV. On Ag(111) [*Giesen et al. (1985)*] the image state lies close to but definitely below the top of the gap ($E_{im} - E_U = -0.23$ eV). The bulk solution is exponentially damped, the matching at the surface is no longer at zero amplitude, this shifts the maximum of the wave function in the region of the image potential further away from the surface. As a consequence, the electron is more likely to be found in a region where the image potential is weaker and, consequently, the binding energy decreases to 0.75 eV. On Pd(111) [*Fischer et al. (1993c)*] the image state is located close to the center of the gap. The damping of the wave function in the bulk is much stronger, the amplitude at the surface has increased which pushes the maximum of the wave function in the vacuum still further out, resulting in a binding energy of 0.56 eV. In the hypothetical case that the image state is located at the bottom of the gap, the solution in the bulk is a p-

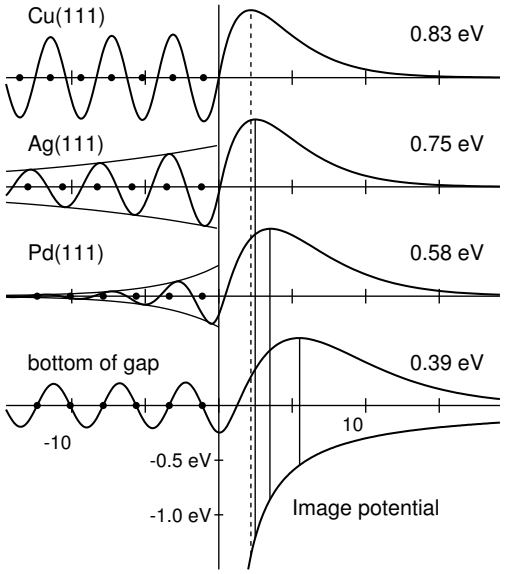

FIG. 17. Wave function of $n = 1$ image states as a function of their energetic position relative to the band gap. The matching conditions at the surface push the maximum away from the surface leading to a decrease in binding energy going from the top to the bottom of the band gap.

		Φ	$E_b(1)$	$E_b(2)$	$E_b(3)$	m^*
Ag(100)	expt.	4.43	0.533	0.162	0.075	1.15
	calc.	4.435	0.529	0.169	0.080	1.0
Ag(111)	expt.	4.56	0.77	0.23	0.10	1.3
	calc.	4.54	0.75	0.21	0.09	1.3
Au(111)	expt.	5.55	0.80	—	—	—
	calc.	—	0.87	0.21	0.09	
Cu(100)	expt.	4.63	0.57	0.18	—	0.9
	calc.	4.62	0.52	0.17	0.08	1.0
Cu(111)	expt.	4.93	0.83	0.25	—	1.0
	calc.	4.89	0.83	0.21	0.09	1.1
Pd(111)	expt.	5.44	0.55	0.15	—	1.0
	calc.	5.46	0.58	0.18	0.08	0.9
Ni(100)	expt.	5.09	0.61	0.18	—	0.95
	calc.	5.09	0.50	0.16	0.08	0.9
Ni(111)	expt.	5.25	0.80	0.25	0.10	1.12
	calc.	5.22	0.64	0.19	0.09	1.0
Co(0001)	expt.	5.20	0.73	0.18	—	—
	calc.	5.22	0.64	0.19	0.09	
Fe(110)	expt.	5.12	0.73	0.18	0.05	—
	calc.	5.15	0.57	0.18	0.08	

TABLE 2. Measured work function Φ and binding energies of the image states for various surfaces. The measured binding energies were used to determine the extrapolated work function within the quantum-defect model. All energies are in eV and the experimental uncertainties are typically ± 0.03 eV. The effective mass m^* for the first image state is in units of the free-electron mass m and carries a typical experimental error of ± 0.1 m. Results of a one-dimensional model calculation are also given. References to the experimental data are given in the text.

like wave function, the matching at the surface occurs at maximum amplitude and the maximum of the wave function in the vacuum is found more than twice as far away from the surface as for Cu(111) at the top of the gap. The potential energy at the maximum of the wave function shows the same trend as the binding energy (dashed lines in Fig. 17). It is not equal to the binding energy because the average distance of the electron lies beyond this point. For the cases near the gap edges the decay length of the wave function into the bulk is over 130 Å. For Ag(111) and Pd(111) the corresponding values are 14.6 Å and 4.0 Å, respectively.

The binding energies of image states on clean metal surfaces determined experimentally are listed in Tab. 2. For the noble metal surfaces the experimental data agree within the limits of error with the results of the calculation described in Sect. 3 2. For Cu(100) the difference between measured and calculated binding energy is marginally outside the error bounds [*Giesen et al. (1987a)*]. The deviation in $E_b(2)$ on Cu(111) is presumably due to space charge because the photon energy exceeded the work function [*Kubiak (1988)*]. For Au(111) the image state is located well above the top of the gap ($E_{im} - E_U = 1.15$ eV) and is, therefore, very broad. The one-dimensional scattering model tends to overestimate the binding energies in this situation. The inclusion of an imaginary part of ~ 0.7 eV to the potential leads to a decaying wave function in the bulk and agreement with the experimental value is obtained. Image states outside band gaps are often called image resonances and have been detected by 2PPE on Cu(110) [*Quiniou et al. (1993)*] and Al(111) [*Bulović et al. (1994)*]. Rather broad peaks were found which do not permit to put a stringent test on the theoretical models [*Jurczyszyn (1991)*].

For the ferromagnets [*Giesen et al. (1986), Schuppler et al. (1990b), Fischer et al. (1990), Fischer et al. (1992), Schuppler et al. (1992)*] the agreement is much less satisfactory. The discrepancy between the measured and the calculated values for the binding energy of the $n = 1$ image state is for all ferromagnetic surfaces at least three times as large as the experimental error. This discrepancy cannot be removed by an adjustment of the band gap parameters within reasonable limits. It is not likely that the d-bands around the Fermi level are responsible for the deviation. A more plausible explanation may be many-body effects described by the self-energy (see Sect. 4 3). The real part of the self-energy is known to be considerable for Fe [*Santoni and Himpsel (1991)*], but negligible for Cu surfaces [*Jacob et al. (1986)*].

The results on binding energies are summarized in Fig. 18 which shows the experimental data relative to the band gap. The results of calculations of the one-dimensional scattering model are shown as lines for Ag(100) and Co(0001), which have the two extreme val-

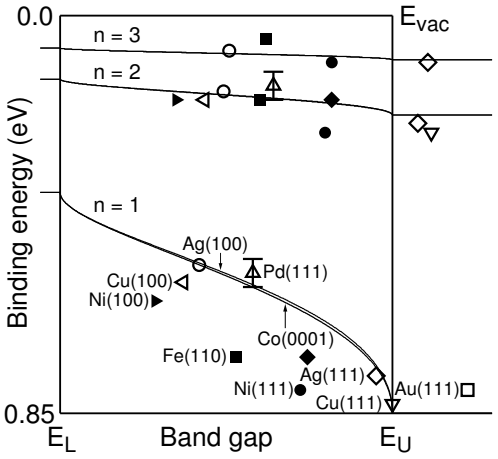

FIG. 18. Measured (symbols) and calculated (lines) binding energies of image states as a function of their energetic position relative to the band gap.

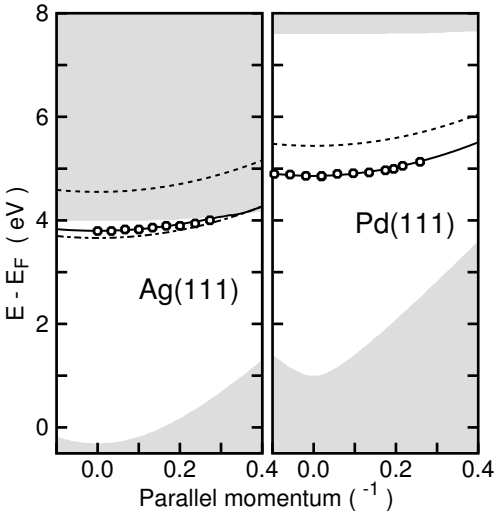

FIG. 19. Dispersion of the image states on Ag(111) [*Giesen et al. (1987b)*] and Pd(111) [*Fischer (1993)*] from experiment (open symbols). The areas outside the band gap where bulk states exist are shaded. Lines show the effective vacuum energy (dashed curves) and the calculated dispersion of the image states (solid lines). The dot-dashed line for Ag(111) is the extrapolation of the free-electron parabola obtained outside the band gap [*Giesen et al. (1987b)*].

ues of the transmission factor in Tab. 1. These curves can be used to obtain the quantum defect a from Eq. 15. The usefulness of the quantum-defect model can also be seen from the extrapolated work function given in Tab. 2 for each surface in the second row.

2. Effective masses

The dispersion of the image states $E_{im}(k_{\|})$ is determined by measuring at off-normal emission (see Fig. 8). The energy associated with the surface k vector is

$$E_{\|} = \hbar^2 k_{\|}^2 / 2m \tag{17}$$

Image states are, therefore, expected to show a parabolic dispersion. This is shown in Fig. 19, where the peak positions of Fig. 8 for Pd(111) [*Fischer (1993)*] have been plotted in the right-hand part and in the same way the data for Ag(111) [*Giesen et al. (1987b)*] in the left-hand picture. The data are fitted by replacing the free-electron mass in Eq. 17 by an effective mass m^*. The experimental results [*Giesen et al. (1987a), Giesen et al. (1987b), Kubiak (1988), Fischer (1993), Starke et al. (1992), Schuppler et al. (1990b)*] are listed in Tab. 2. They are equal to the free-electron mass within the limits of error for all surfaces except Ag(111) where $m^* = 1.3\ m$ is found. The data points in Fig. 19 lie clearly above the free-electron parabola. This can be accounted for by the change of the position of the image state relative to the gap which has the strongest effect near the band edge (see Fig. 18). The effective masses calculated by a quantitative evaluation of this shift are also listed in Tab. 2. They agree with the experimental data within the limits of error.

The dispersion can be only described by an effective mass close to the free-electron value, if the electron can move freely parallel to the surface. This has been demonstrated on a stepped Cu(100) surface where a free-electron dispersion was found in the direction parallel to the steps [*Ortega et al. (1994)*]. Perpendicular to the steps no dispersion was found and attributed to a one-dimensional localization. Similar observations will be discussed in Sect. 6.

3. Lifetimes

Image states are expected to have a much longer lifetime than excited bulk states. They should be only weakly coupled to the bulk as the electron is located in front of the surface. The lifetime of excited bulk states is limited by decay via electron-hole-pair creation. Image states can decay by the same process by means of their coupling to the bulk. A measure of this coupling is the penetration p of the image state into the bulk [*Andres et al. (1987)*], i. e., part of the wave function in the bulk, to the left of the surface (see, e. g., Fig. 17)

$$p = \int_{-\infty}^{0} \psi^* \psi \, dz \; / \int_{-\infty}^{+\infty} \psi^* \psi \, dz \tag{18}$$

The lifetime τ can be determined either directly by time-resolved spectroscopy or by the resulting lifetime broadening Γ via measurement of the linewidth or by line-profile analysis (see Sect. 2 1 5). In this chapter Γ will generally be given as a measure of the lifetime.

	$p \cdot \Gamma_b$	$\Gamma(1)$	$\Gamma(2)$	Ref.
Ag(100)	22	21± 4	3.7 ± 0.4	[*Schuppler et al. (1990a)*]
Ag(111)	123	45±10	$< \Gamma(1)$	[*Fischer (1993)*]
Au(111)	617	160±40	—	[*Reuß (1994)*]
Cu(100)	18	28± 6	$< \Gamma(1)$	[*Wallauer*]
Cu(111)	421	85±10	—	[*Wallauer*]
Pd(111)	40	70±20	$< \Gamma(1)$	[*Fischer et al. (1993c)*]
Ni(100)	24	70± 8	$< \Gamma(1)$	[*Schuppler et al. (1992)*]
Ni(111)	40	84±10	12 ± 10	[*Fischer et al. (1991)*]
Co(0001)	40	95±10	18 ± 13	[*Fischer et al. (1992)*]
Fe(110)	95	130±30	25 ± 15	[*Fischer et al. (1992)*]

TABLE 3. Lifetime broadening Γ (in meV) of image states on metals. The third and fourth columns show the experimental linewidths for the first and second image state. The second column gives the heuristic estimate of the linewidth for the $n = 1$ image state using penetration and bulk linewidth. The last column gives the references to the experimental data.

In a heuristic approach it is plausible to set the lifetime broadening of the image state to $p \cdot \Gamma_b(E)$, i. e., the penetration into the bulk multiplied with the broadening of a bulk state of the same energy. The linewidth of bulk states increases linearly with increasing distance from E_F: $\Gamma_b(E) = \alpha \cdot |E - E_F|$. The coefficient α has been determined experimentally as 0.13 for Ag and Cu [*Goldmann et al. (1991)*], 0.18 for Ni [*Eberhardt and Plummer (1980)*] and 0.6 for Fe [*Santoni and Himpsel (1991)*]. The same value as for Ag and Cu was used for Au. For Pd and Co, $\alpha = 0.18$ was assumed because the band structure is similar to Ni. With these values for α, estimates for $p \cdot \Gamma_b$ were obtained for the $n = 1$ image states. They are listed in the second column of Tab. 3. The penetration p was calculated using Eq. 18 and calculated wave functions (see Fig. 17). In the third column the experimental results are presented. All the data $\Gamma(1)$ for the $n = 1$ states were obtained by line-profile analysis. For the close-packed surfaces with occupied surfaces states (Ag, Au, Cu, Ni, and Co), $\Gamma(1)$ was obtained off-resonance. In resonance a smaller linewidth is obtained [*Merry et al. (1993), Reuß (1994)*]. The most striking example is Cu(111), where 16 meV was obtained from a line-shape analysis in resonance [*Schuppler et al. (1992)*] compared to 85 meV off resonance in Tab. 3 (see also Fig. 5). The spectra shown in Fig. 16 for the (111) surfaces were measured under resonance conditions. The lifetimes in Tab. 3 range from 31 fs for Ag(100) to 4 fs for Au(111). Even for Ag(100), where time-resolved spectroscopy has yielded 15 fs $< \tau <$ 35 fs [*Schoenlein et al. (1988)*], the result obtained by line-profile analysis [*Schuppler et al. (1990a)*] is more accurate and reliable. The $n = 2$ image states are expected to have a considerably longer lifetime as they are more weakly coupled to the bulk. The experimental results listed in the fourth column of Tab. 3 show that this is actually true; in most cases the answer is only qualitative. The best result, for Ag(100), has been obtained by time-resolved spectroscopy [*Schoenlein et al. (1990)*] which is clearly superior in this range of lifetimes.

A comparison of the second and third column of Tab. 3 shows that the heuristic estimate in most cases yields the right order of magnitude. For Ag(100) the agreement is perfect, for Cu(100) it is still fair. For the other surfaces the heuristic approach needs to be corrected for effects which have not been taken into account [*Schuppler et al. (1992)*]. The most drastic discrepancies occur for the (111) surfaces of Ag, Au, and Cu. The fact that the width in these cases is much smaller than estimated is explained as follows: For these surfaces the gap extends below E_F (see Fig. 15) which means there are no unoccupied final states available for the decay of the image state with $\Delta k_\parallel = 0$. The small width results from the blocking of the main part of the decay channel, in this case. It should be added that the penetration was calculated without the additional damping of the wave function by an imaginary part of the potential.

For Pd(111) and the surfaces of the ferromagnets another effect has to be corrected for: unoccupied surface states or surface resonances can contribute considerably to the decay of an image state because the overlap is much larger than with bulk states. This has been proven experimentally for Ni(111) where a quenching of the surface state leads to a reduction of the width of the image state [*Fischer et al. (1990)*]. A similar effect is presented for Au on Pd(111) in Sect. 5 2 1.

A more fundamental calculation of the lifetime of image states has to take into account that the image potential arises from the screening of the charge of the electron outside the metal surface by the electrons of the metal. Consequently, the image potential is a many-body effect at the surface. Theoretical models [*Echenique et al. (1985), Eguiluz and Hanke (1989)*] have been developed to describe the dynamic response of the metal surface to the field of an electron outside the metal. A self-consistent potential has been derived which can be interpreted via a self-energy of the image-state electron. The real part of the self-energy describes an energy shift due to the many-body interaction of the image-state electron with the metal electrons. The imaginary part accounts for inelastic processes which lead to the finite linewidth of image states. *Echenique and Pendry (1990)* have calculated the linewidth of image states using a free-electron description for the metal and the two-band model for the penetration. They find for the $n = 1$ image state on Ag(100) $\Gamma = 8$ meV [*Echenique et al. (1985)*]. With correct band-structure parameters 20 meV and 40 meV is obtained for Ag(111) and Cu(111) [*Andres et al. (1987), Schuppler et al. (1992)*]. While for Ag(100) the heuristic estimate yields a result closer to the experimental findings, the more fundamental calculation leads to better agreement for Ag(111) and Cu(111). Obviously more refined calculations are needed to account for all the experimental results listed in Tab. 3.

5. IMAGE STATES ON METAL OVERLAYERS

For deposition of a metal overlayer on a metal substrate the concept of the image charge still applies, and image states should be expected. The interesting question is: How do the image states of the substrate change with coverage and develop into the corresponding ones of the overlayer material for a thick film? The thickness at which the image-state series of the overlayer material is observed can give direct information about the penetration of the wave function of the image state into the metal. The observed behavior will depend on the growth mode and the surface morphology.

1. Local work function

1. Ag on Pd(111)

The first system studied by two-photon photoemission was Ag on Pd(111) [*Fischer et al. (1993c)*]. For this system a large work-function difference and, consequently, a large difference in the energies of the image states relative to E_F exists. Spectra for Ag coverages between 0 and 2.0 monolayers (ML) on Pd(111) are shown in Fig. 20 on an energy scale relative to E_F. A new state at

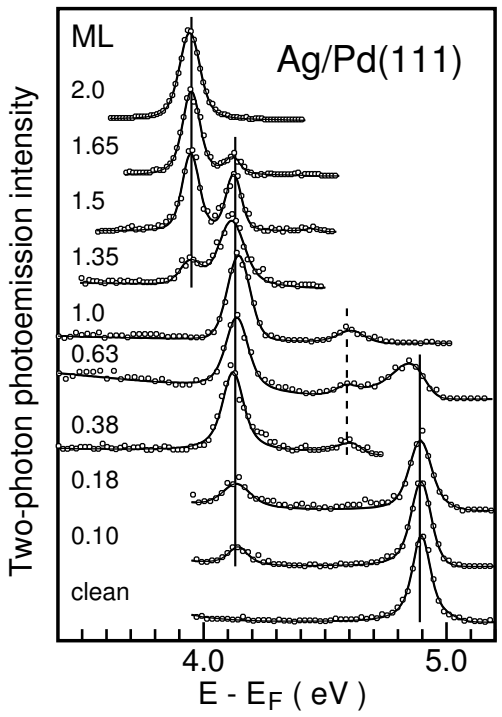

FIG. 20. Series of two-photon photoemission spectra showing the evolution of the image states as a function of Ag coverage on Pd(111) [*Fischer et al. (1993c)*]. The energy scale is relative to E_F.

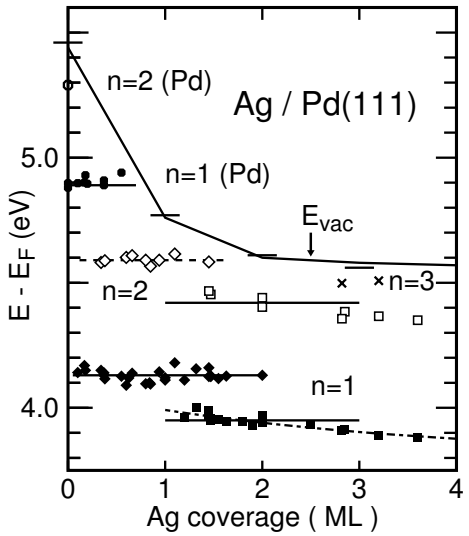

FIG. 21. Energies of the image states as a function of the Ag coverage on Pd(111) [*Fischer et al. (1993c)*]. Average values are shown by the horizontal lines (solid: $n = 1$, dashed: $n = 2$). The dot-dashed line is the result of a fit to data for the $n = 1$ state for coverages above 2 ML and converges to the value for bulk Ag. As symbolized by a line the vacuum energy E_{vac} decreases linearly for coverages between the completed layers.

an energy of 4.13 eV appears already at 0.1 ML. This peak increases in intensity relative to the $n = 1$ state for the clean surface at 4.89 eV which has disappeared at 1.0 ML. For coverages above 1.0 ML, a new peak at 3.95 eV is visible which remains the only peak at 2.0 ML. These new states lie independent of coverage always at a fixed energy relative to E_F. They are the only states observed at full monolayer coverages and are the image states for 1 ML and 2 ML of Ag on Pd(111). The assignment of the states to image states is confirmed by the observation of a series of states. In Fig. 20 the $n = 2$ state for 1 ML Ag can be seen at 4.59 eV which is below the $n = 1$ state for clean Pd(111). The narrow linewidth observed at all coverages is also characteristic for image states. The fact that for complete layers only one state is observed confirms the layer-by-layer growth [*Eisenhut et al. (1993)*]. For intermediate coverages, two $n = 1$ states can be observed from areas with different layer thicknesses.

The energies of all observed states relative to E_F are plotted in Fig. 21 as a function of Ag coverage. The energies of the various states stay constant within the respective coverage ranges. The vacuum energy determined from the low-energy cutoff of the spectra varies linearly between the coverages of the completed monolayers. The resulting binding energies would also vary linearly with coverage and extremely small values outside the range of Eq. 15 would occur. Therefore, the Fermi energy is the correct energy reference. It permits an easy interpretation of the data and will be used throughout

most of the following sections. The linear decrease of the work function reflects an average over the patches with different thicknesses of the Ag film. The image states are closer to the surface and 'feel' a local work function corresponding to the individual patch at which the electron is trapped. The area over which the work function is averaged depends on the distance of the test electron from the surface [*Wandelt (1987)*]. The local work function obtained from image states is characteristic for the homogeneous patch where the electron is trapped. It is not influenced by defects and inhomogeneities of the surface and can give more reliable values for the work function [*Fischer et al. (1993a), Fischer et al. (1993c)*].

For completed layers there is no difference between the macroscopic and the local work function. This can be checked by the convergence behavior of the series of image states using the quantum-defect model described in Sect. 3 3. The values for the (local) E_{vac} extrapolated in this way agree very well with the work function measured for the completed layers [*Fischer et al. (1993c)*] as indicated by the short horizontal lines along the curve E_{vac} in Fig. 21. Note that the extrapolation can be done at any coverage yielding the appropriate local work function.

2. Ag on Au(111)

A layer-by-layer growth mode has been observed for the deposition of Ag on Au(111) [*Borensztein et al. (1987), Chambliss and Wilson (1991)*]. The concept of the local work function presented in the preceding section for the case of Ag on Pd(111) should be applicable to the Au substrate. The work function and the energy of the first image state of Au(111) differ by ≈ 0.1 eV from the corresponding values of Pd(111) (see Tab. 2). The experimental data [*Reuß (1994)*] are plotted in Fig. 22 as a function of Ag coverage. The work function decreases linearly between the full monolayer coverages. The image state for 1 ML Ag on Au(111) is seen between 0.1 and 1.8 ML at an energy of 4.23 eV relative to E_F. From the second monolayer on, the $n = 2$ state at 4.42 eV can be observed in addition to the $n = 1$ image state at 3.91 eV. The energy range shown in Fig. 22 lies entirely outside the band gap of Au(111). For clean Au(111) only a broad image-state peak is found and no significant resonance enhancement with the occupied surface state is observed. The $n = 2$ state could not be seen at all, which might be due to the absence of available initial states. It is, therefore, remarkable that a resonance behavior and the $n = 2$ state can be already observed at a coverage of 2 ML of Ag. The absence of a band gap of the Au(111) substrate leads to a large penetration of the wave function resulting in a considerable linewidth. The linewidth has dropped into the range known for Ag(111) only for coverages above 4 ML [*Reuß (1994)*].

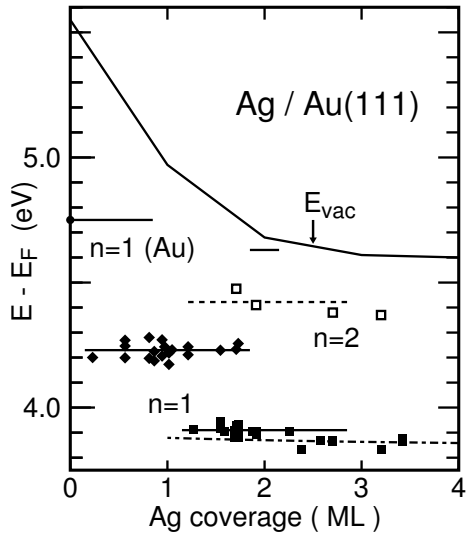

FIG. 22. Energies of the image states as a function of the Ag coverage on Au(111) [*Reuß (1994)*]. The horizontal lines are guides for the eyes. The uppermost curve describes the vacuum energy.

3. Ag on Cu(111)

Two-photon photoemission spectra for the clean Cu(111) surface as well as for the Ag-covered surface are shown in Fig. 23 [*Wallauer and Fauster (1995)*] plotted relative to E_F. The first image state of Cu(111) is visible at an energy of 4.11 eV relative to E_F up to a Ag coverage of 0.9 ML. The adsorbate-induced features are the $n = 1$ and $n = 2$ image states at at 3.87 eV and 4.38 eV, respectively. At a coverage of 1 ML only the image states of 1 ML Ag on Cu(111) is observed, as expected for layer-by-layer growth. The strong relative intensity of the $n = 2$ state results from a resonant excitation out of the occupied surface state of 1 ML Ag on Cu(111). At the same photon energy, the resonance between the occupied surface state and the first image state occurs on the clean Cu(111) surface (see Fig. 5). This explains the strong intensity of the substrate peak relative to the monolayer features in Fig. 23.

In Fig. 24 the energies of all observed peaks relative to E_F are shown as a function of coverage. The vacuum energy, shown by the upper solid line decreases linearly up to a coverage of 1 ML, where it has almost reached the value for Ag(111). The data show that all detected image states remain at their energetic position with increasing coverage. This can easily be understood with the concept of the local work function. The 2PPE results indicate clearly the growth of a smooth first monolayer in agreement with previous studies [*Shapiro et al. (1986), Borensztein et al. (1987), McMahon et al. (1992), Mottet et al. (1992)*]. For Ag on Cu(111) the occupied surface

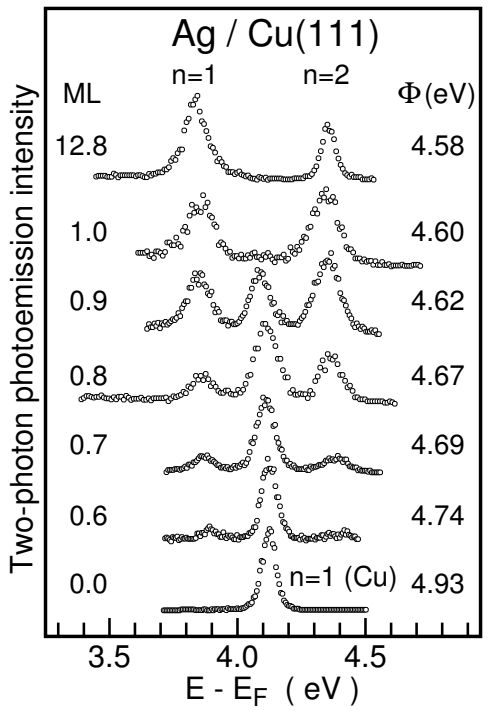

FIG. 23. Series of two-photon photoemission spectra of Cu(111) with increasing Ag coverage [*Wallauer and Fauster (1995)*]. The $n = 1$ image state of Cu(111) decreases in intensity with increasing Ag coverage while the emission out of the $n = 1, n = 2$ image states of Ag on Cu(111) increases. The coverage and the work function Φ are given at the left and right side of each spectrum, respectively.

states show a similar behavior with coverage as the image states (photoemission spectra not shown here, compare to [*Shapiro et al. (1986)*]).

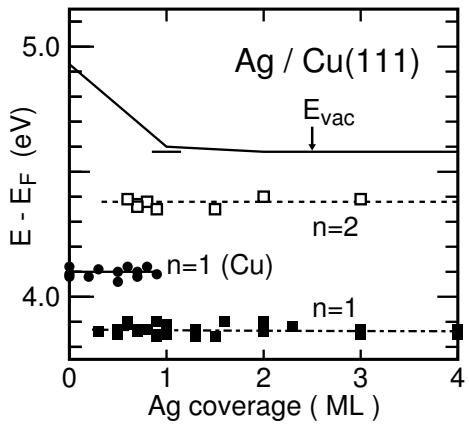

FIG. 24. Energies of the image states as a function of the Ag coverage on Cu(111) [*Wallauer and Fauster (1995)*]. The horizontal lines are guides for the eyes. The uppermost curve describes the vacuum energy which shifts linearly between 0 and 1 ML coverage and reaches, within the limits of errors, at 1 ML already the Ag(111) bulk value.

4. Estimate of the wave function

On Pd(111) and Au(111) the image states for 1 and 2 ML Ag could be clearly resolved. For coverages above two monolayers a weighted average of the energies for the nearest completed layers is measured due to the limited energy resolution. For Ag on Pd(111) the energies of the $n = 1$ states can be fitted very well for coverages $\Theta > 1.2$ ML by (see dot-dashed line in Fig. 21).

$$E(1) = 3.80 \text{ eV} + 0.26 \text{ eV} \cdot \exp(-\Theta/3.2 \text{ ML}) \ . \quad (19)$$

In first-order perturbation theory the energy correction as a function of coverage can be estimated [*Fischer et al. (1993c)*]. The system of j layers of Ag on Pd can be regarded as a Ag crystal whose potential V_{Ag} is changed to the Pd potential V_{Pd} after j layers. Above 2 ML the energies of the $n = 1$ states are just below the upper edge of the Ag band gap and the wave function for a thick Ag film can be approximated (compare to Fig. 17) by

$$\psi(z) = \exp(z/\lambda)\sin(\pi z/d) \ , \ z < 0 \ . \quad (20)$$

For Ag(111) the layer separation d is 2.36 Å and the decay length λ can be estimated as 6.1 ML [*Smith (1985), Fischer et al. (1993c)*]. The periodic potential

$$V(z) = E_C - (E_U - E_L)\cos(2\pi z/d) \quad (21)$$

yields a complex band structure almost identical to the solution of the one-dimensional scattering model (Sect. 3 2 2, Fig. 13, and [*Fauster (1994)*]. The energy correction to the state described by the wave function Eq. 20 can then be estimated in first-order perturbation theory to

$$\langle\psi|\Delta V|\psi\rangle \ / \ \langle\psi|\psi\rangle \approx \Delta E_C + (\Delta E_U - \Delta E_L)/2 \ , \quad (22)$$

where the energy differences according to Eq. 21 have to be inserted. Note that the Fermi energy is the proper level of reference here, because the wave function in the metal is being considered. Using the parameters for Ag(111) and Pd(111) from Tab. 1 a perturbation energy of

$$\langle\psi|V_{\text{Pd}} - V_{\text{Ag}}|\psi\rangle \ / \ \langle\psi|\psi\rangle = 2.6 \text{ eV} \cdot \exp(-2j/\lambda) \quad (23)$$

is obtained. This expression predicts the energy correction to decay on a length scale of $\lambda/2 = 3.0$ ML, which is in good agreement with the experimental value. The prefactors differ by a factor of ten, which arises because only the wave function inside the metal (Eq. 20) has been evaluated. The proper normalization of the complete wave function results in a 10% probability to find the electron inside the crystal. The calculated wave function

shown in Fig. 17 for Ag(111) has a 25% probability inside the crystal. The estimate of the probability relies on differences of the potential parameters in Eq. 22 which introduces a relatively large uncertainty and explains the discrepancy. The decay length can be obtained without parameters from the experimental data alone and is, consequently, much more reliable. It should be noted that this constitutes an example for using perturbation theory to obtain the wave function from the energy corrections.

The same analysis should be applicable to the data for Ag on Au(111) and Cu(111). The energy of the $n = 1$ state changes by less than 0.05 eV between 2 ML and the thick films as indicated by the dot-dashed lines in Figs. 22 and 24. It is, therefore, not possible to extract a reliable decay length or prefactor (even when the decay length is fixed to the value obtained on Pd(111)). The parameters of Tab. 1 predict prefactors of -1.0 and -0.3 eV for Au(111) and Cu(111), respectively. These values are considerably smaller than on Pd(111), but would imply a slight increase of the image-state energy. For Au(111) the work function approaches the asymptotic value relatively slowly which might counteract the predicted increase. In this case, the assumption of a wave function independent of energy (Eq. 20) might be questionable. Calculations within the one-dimensional scattering model take the variation of the wave function and the work function into account and yield much better agreement with the experimental results (see the following Sect. 5 1 5 and Tab. 4).

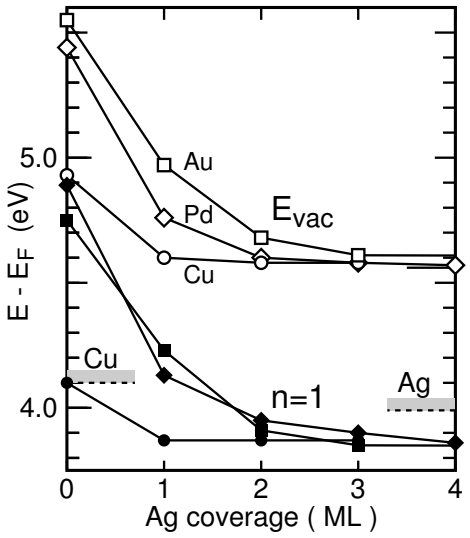

FIG. 25. Work function and energies of the $n = 1$ image states as a function of the Ag coverage on the (111) surfaces of Au, Pd, and Cu. The dashed lines and shaded areas indicate the upper gap edges for Cu(111) and Ag(111). The energy range lies completely above the Au(111) band gap and inside the Pd(111) band gap.

5. Comparison

The three Ag overlayer systems presented in the preceding sections have the layer-by-layer growth in fcc(111) orientation on the fcc(111) substrate in common. In all cases the concept of the local work function could be applied, which implies that relatively large Ag islands form at room temperature (see Sect. 5 3 3). The work function and the energy of the $n = 1$ image state relative to E_F are for Ag(111) lower than for any of the substrates. Therefore, a decrease of these quantities with coverage is observed in Fig. 25 which summarizes the experimental data for the monolayer coverages. The asymptotic values are approached very rapidly, and most of the variation occurs within two monolayers. Between Ag and Cu(111) the differences are so small that the Ag values are already obtained at 1 ML. This is related to the fact that the work-function decrease brings the $n = 1$ image state from the edge of the Cu(111) band gap (shaded area in Fig. 25) into the band gap at a comparable position as for Ag(111). Even though the behavior for Pd(111) and Au(111) looks very similar, there is an important difference: the energy range shown in Fig. 25 lies completely inside the Pd(111) band gap and completely above the Au(111) band gap. This implies that the wave function can penetrate far into the Au substrate, whereas it decays rapidly into the Pd(111) crystal (see Fig. 17). Another consequence is that there occurs almost no change in binding energy for Ag on Au(111). For Pd(111) the total change in binding energy amounts to 0.22 eV. Much thicker films are required to adjust the phase of the wave function at the surface, which is necessary to change the binding energy (see Fig. 17 and Sect. 3 3).

Calculations within the one-dimensional scattering model with its extension to overlayers from Sect. 3 2 4 reproduce the experimental results for the image-state energies very well, as can be seen in Tab. 4. The measured values for the work function and the band parameters from Tab. 1 are used. The disagreement found for Ag on Au(111) is a carry-over from the substrate calculation. The absence of the band gap and the resulting large penetration make the maximum in the inverse determinant (compare Sect. 3 2 3) rather broad, as expected for an image resonance. A tendency to overestimate the binding energies is found for states outside the band gap in the one-dimensional scattering model. Better agreement with the experimental data can be achieved by an imaginary part of 0.4 eV of the potential V_C. This is true for the complete coverage range, because the decay of the Ag(111) wave function in the band gap is not much influenced by such a complex potential. Imaginary parts to the potential of the same magnitude are also included in calculations within the one-step model of photoemission [*Graß et al. (1993)*].

2. Image states and quantum well states

For the Ag overlayers, discussed in the preceding section, the band gap of Ag(111) falls in the energy range relevant to the image states. A different situation occurs for Au overlayers with the band gap at lower energy. The image-state wave function might penetrate the overlayer. If it has to decay rapidly into the substrate a large reflectivity occurs at the interface. This might lead to standing waves in the overlayer, also known as quantum well states. The interesting problem is the influence of the quantum well on the image states.

1. Au on Pd(111)

The ideal system to study this question is Au on Pd(111) [*Fischer and Fauster (1995)*]. There is a large band gap around E_{vac} for Pd, whereas the upper edge of the band gap for Au is ~ 2 eV below E_{vac} (Fig. 27). The work function and the energy of the first image state relative to the Fermi level E_F are very similar for Pd(111) and Au(111) (see Tab. 2 and [*Fischer et al. (1993c), Fischer and Fauster (1995), Reuß (1994)*]). Consequently, only small variations of these quantities with coverage are expected. Due to the small lattice mismatch ($\approx 5\%$) between the two fcc materials epitaxial growth is expected. At room temperature a layer-by-layer growth has been reported [*Kuk et al. (1983), Jaklevic (1984)*] with pseudomorphic Au layers for coverages up to 3 monolayers (ML) [*Eisenhut (1992)*].

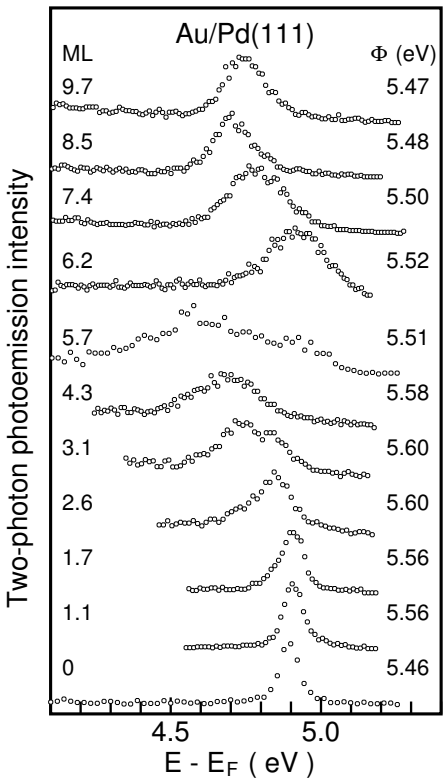

FIG. 26. Series of two-photon photoelectron spectra with increasing Au coverage on Pd(111) [*Fischer and Fauster (1995)*]. The energies of the unoccupied states are plotted relative to the Fermi level. The coverage and work function are given to the left and right of each spectrum, respectively.

		clean	1 ML	2 ML	3 ML	4 ML	film
Ag	Φ	5.44	4.76	4.60	4.58	4.57	4.55
on	exp.	4.89	4.13	3.95	3.90	3.86	3.80
Pd	calc.	4.86	4.13	3.93	3.88	3.86	3.80
Ag	Φ	5.55	4.97	4.68	4.61	4.60	4.59
on	exp.	4.75	4.23	3.91	3.85	—	3.80
Au	calc.	4.69	4.13	3.87	3.82	3.82	3.83
Ag	Φ	4.93	4.60	4.58	4.58	4.58	4.58
on	exp.	4.10	3.87	3.87	3.87	3.85	3.80
Cu	calc.	4.10	3.85	3.83	3.83	3.83	3.82
Au	Φ	5.47	5.56	5.56	5.60	5.58	5.47
on	exp.	4.89	4.88	4.86	4.83	4.70	4.75
Pd	calc.	4.89	4.88	4.79	4.76	4.67	4.60
Au	Φ	4.93	5.18	5.36	5.47	5.53	5.55
on	exp.	4.10	4.34	4.47	—	—	4.75
Cu	calc.	4.10	4.27	4.39	4.42	4.11	4.69
Co	Φ	4.93	4.98	5.03	5.08	5.10	5.20
on	exp.	4.10	4.38	4.43	4.44	4.47	4.47
Cu	calc.	4.10	4.26	4.37	4.43	4.46	4.56

TABLE 4. Measured work function Φ and energies of the first image states for various metal-on-metal systems with fcc(111) orientation. All energies are in eV relative to E_F and the experimental uncertainties are typically ±0.03 eV. Results of a one-dimensional model calculation are also given.

A series of spectra for Pd(111) with Au coverages ranging from 0 to 10 ML is shown in Fig. 26. The work function is given to the right of each spectrum and shows little variation as expected. The observed increase indicates a smooth surface in agreement with a layer-by-layer growth mode [*Kuk et al. (1983), Jaklevic (1984)*]. For a rough surface a lowering of the work function would be expected [*Wandelt (1987)*]. For coverages $\lesssim 4.5$ ML the increase might be correlated with the lateral compression of the pseudomorphic Au layers on Pd(111) [*Eisenhut (1992)*].

The image states show much more dramatic changes as a function of coverage in contrast to the work function. The sharp peak at 4.89 eV for clean Pd(111) shows no shift in energy for small coverages. The peak becomes narrower with an intrinsic linewidth of 40 ± 20 meV at 1 ML compared to 70 ± 20 meV for the clean surface. The explanation is the quenching of the unoccupied surface state of Figs. 3 and 7 which eliminates an important decay channel for the image state [*Schuppler et al. (1992)*]. For coverages above 1 ML the peak broadens considerably and shifts to lower energy. At 5.7 ML intensity in the energy range from 4.3 to 5.1 eV is seen. The upper limit is determined by excitation of electrons from E_F

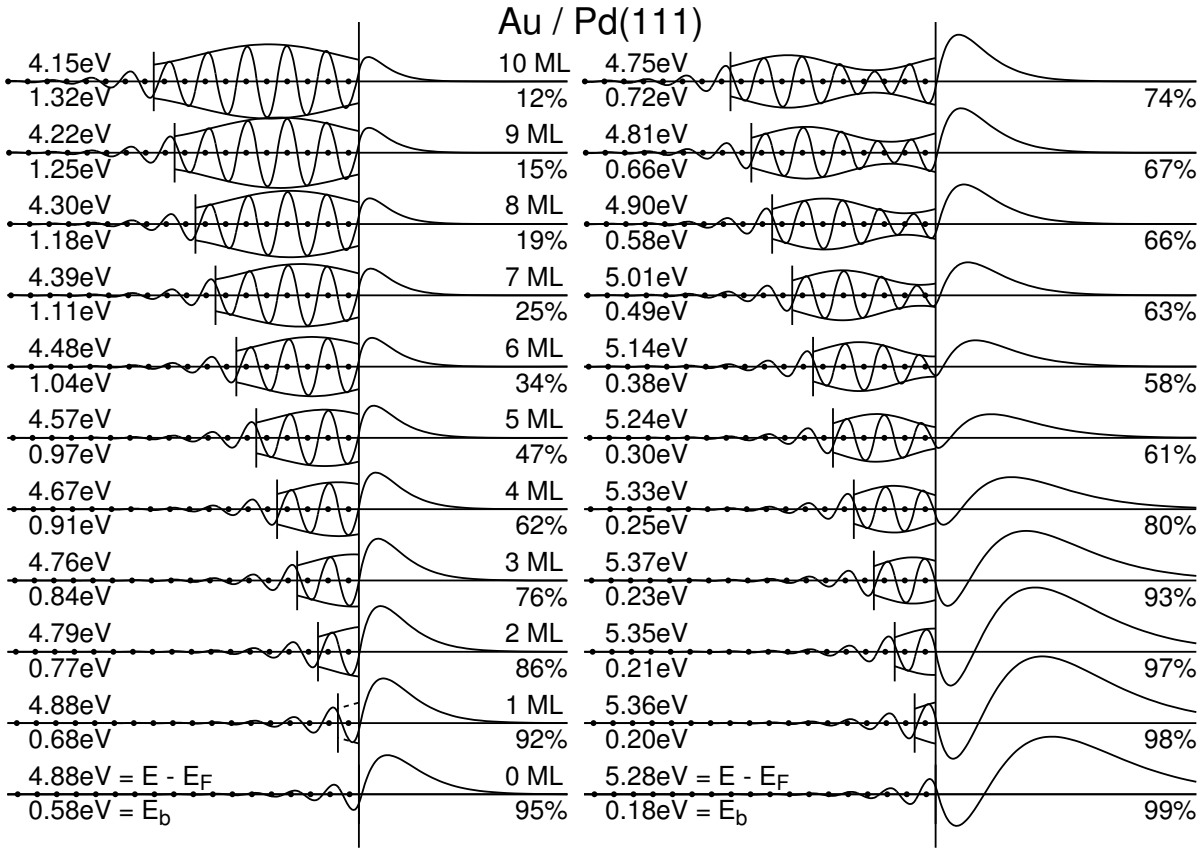

FIG. 28. Calculated wave functions for Au films of various thicknesses on Pd(111). The dashed lines represent the envelope functions [*Smith et al. (1994), Ortega et al. (1993)*] for the quantum well states in the Au layer. The position of the atoms is indicated by the filled circles. The energies of the states and the probability to find the electron outside the surface are given.

by the frequency-doubled photons. The maximum intensity occurs at a binding energy of ~ 1 eV. This value is outside the regime covered by positive quantum defects

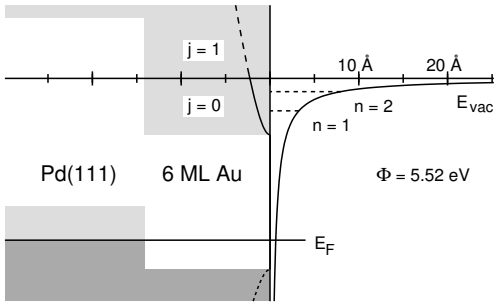

FIG. 27. Schematic image potential and projected bulk bands (shaded areas) for 6 ML of Au on Pd(111) [*Fischer and Fauster (1995)*]. The energy bands of Au(111) are indicated by the dashed lines with the origin at the interface and the zone boundary at the surface of the Au layer. By a variation of the phases ϕ in Eq. 24 the energy ranges indicated by the short and long dashes are covered by the $j = 0$ and $j = 1$ quantum well states, respectively.

a in Eq. 15. At 6.2 ML only one peak at 4.93 eV remains which shifts down in energy until a spectrum similar to the clean Au(111) surface (see Fig. 16) is obtained.

The experimental findings cannot be attributed to the morphology of the film or interpreted within the framework of the local work function [*Fischer and Fauster (1995)*]. The explanation for the observed behavior with coverage is related to the larger penetration. The wave function of the electron can be reflected at the interface between the Au film and the Pd substrate. The resulting standing waves correspond to quantum well states. In an overlayer of thickness d the associated wave vector is

$$k = (2\pi j + \phi_B + \phi_C)/2d\,, \quad j = 0, 1, 2, \ldots \tag{24}$$

The number of extrema of the wave function in the quantum well is $j + 1$. The phases ϕ_B and ϕ_C describe the phase shifts (see Sect. 3 3) at the reflection by the vacuum barrier and the crystal. The energy of a state with wave vector k is $E = \hbar^2 k^2/2m^*$ relative to the bottom of the quantum well with an effective mass m^* describing the motion of the electron in the solid. For an overlayer the bulk band structure can be used with an appropriate choice of the band edge as the origin of the energy and

the wave vector scale [*Smith et al. (1994), Ortega et al. (1993)*]. In this case k represents the wave vector of the envelope function. Figure 27 shows the energy ranges spanned by the $j = 0$ and $j = 1$ states for a layer thickness of 6 ML and a variation of the total phase $\phi_B + \phi_C$ between 0 and 2π. The upper band edge and the zone boundary are chosen as the origin of the energy and wave vector scale, respectively.

For 6 ML the energy of the $j = 0$ state is expected to fall in the energy range of the image states as indicated by the short-dashed energy band shown for the Au layer in Fig. 27. The energy depends on the phase shifts in Eq. 24. The strong interaction between the image state and the quantum well state in the Au layer is illustrated in Fig. 28 by the wave functions calculated within the one-dimensional scattering model [*Fauster (1994)*]. The left (right) column shows the states with the lowest (second lowest) energy. The states do not necessarily correspond to the $n = 1(2)$ image states. An example is the wave function of the second state for 6 ML Au on Pd(111) which is in the vacuum region very similar to the $n = 1$ wave function on the clean Pd(111) surface. Both states have also very similar binding energies. The lowest states (left column of Fig. 28) have for Au coverages above 3 ML a binding energy above 0.85 eV, in agreement with the experimental data and outside the regime of positive quantum defects in Eq. 15. Their wave function extends much less into the vacuum, so it has more the character of a quantum well state which is influenced by the image potential. This is also seen by the probability of finding the electron in the image-potential region which decreases for the lowest states rapidly with increasing Au coverage. The situation is different for the states of next higher energy, shown in the right column of Fig. 28. The probability decreases with coverage and passes through a minimum at 6 ML. Above this coverage the binding energies of the states fall into the range of the $n = 1$ states of Eq. 15. The wave functions on the vacuum side are identical to the wave functions on clean surfaces with corresponding binding energy (compare Fig. 17).

The detailed behavior of the calculated states is shown in Fig. 29. With increasing coverage the lowest state is pulled down in energy and becomes more a quantum well state at higher coverages. In the calculations this can be checked because their energy is less influenced by the work function in contrast to image states. The second state shows a small maximum due to the initial work function increase before it is pulled down and acquires the $n = 1$-image-state character above 6 ML. There is generally good agreement with the experimental data. The spectra have been fitted with two peaks and the size of the symbols indicates the relative intensity at each coverage. The quantum well states are seen only with low intensity for coverages above ~ 6 ML. This is probably due to a shorter lifetime of these states which have most of their wave function in the metal. In the calculations this can be modeled by the introduction of an imaginary part of the potential. A value of 0.4 eV (see Sect. 5 1 5) makes the lowest state disappear for higher coverages (see dashed lines in Fig. 29). The imaginary part has only little influence on the calculated energies.

The presented example shows that the distinction between image states and quantum well states becomes difficult when they are close in energy. A simple criterion might be the probability to find the electron outside the layer but this quantity varies with layer thickness. It also depends on the energetic position relative to band gap of the substrate and is particularly high for Pd(111) with E_{vac} near the center of the band gap. A binding energy of more than 0.85 eV implying a negative quantum defect a in Eq. 15 gives an unambiguous test to exclude image states. For surface states in Shockley-inverted band gaps [*Smith (1985)*] the wave function and its derivative always have opposite signs at the interface (see Fig. 17). The metal overlayer introduces a phase shift which changes with coverage (and energy) leading to a different situation as can be seen in Fig. 28. It is worthwhile to point out that the image potential outside the surface is independent of the substrate or overlayer. The changes in the energies are not due to a hybridization between electronic states of the surface and the quantum well. The energies of both states are not fixed in energy and shifted by the interaction, but can vary over a considerable energy range. The relevant property is the boundary condition at the surface (see Sects. 3 2 3 and 3 3). This leads to the somewhat surprising fact that

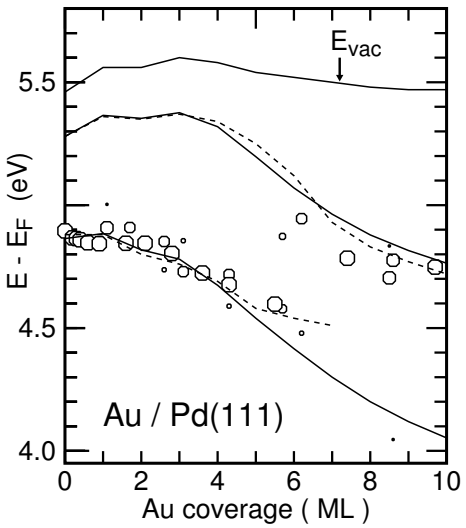

FIG. 29. Measured vacuum energy, experimental and calculated energies of the unoccupied states as a function of Au coverage on Pd(111) [*Fischer and Fauster (1995)*]. All energies are relative to the Fermi level. The size of the symbols indicates the relative peak intensities for spectra where two peaks are observed. The dashed lines are calculated with an imaginary part of the bulk potential.

the image state as an extreme case of a surface state actually carries information on the properties of the bulk substrate or an overlayer.

2. Au on Cu(111)

The growth mode of ultrathin Au films on single crystal Cu(111) surfaces at room temperature has not been studied in detail with modern surface-science techniques. Gold and copper are miscible and a surface alloy has been observed at elevated temperatures [*Fujinaga (1977), Xu et al. (1990)*]. Photoemission, Auger electron spectroscopy, and LEED indicate no surface-alloy formation at room temperature [*Wallauer and Fauster (1995)*]. The growth of three-dimensional islands is supported by the observation of two sets of LEED spots at Au coverages close to 1 ML on Cu(111). They correspond to the (1×1) structures of Cu(111) and a hexagonal layer with the lattice spacing of Au(111).

The two-photon photoemission spectra for Au adsorbed on Cu(111) are complicated to analyze [*Wallauer and Fauster (1995)*]. The image states of Au(111) do not lie in a band gap of the projected bulk band structure and have a reduced lifetime. This leads to much broader peaks in the spectra even for thin films [*Fischer and Fauster (1995)*]. Additional complications arise from a strong signal of the occupied surface state and from the absence of a resonance effect for Au(111) [*Reuß (1994)*]. A careful study of spectra for many photon energies leads to an identification of the image-state features, as shown in Fig. 30. The $n = 1$ image state of the substrate is observed as well as two features which are denoted by 1 ML Au at 4.34 eV and 2 ML Au at 4.47 eV, respectively. The assignment of these peaks to $n = 1$ image states on 1 and 2 ML high gold islands is supported by the identification as unoccupied states due to their photon energy dependence. The fact that the $n = 1$ state of the Cu(111) substrate is visible up to a coverage of 1.7 ML and the simultaneous observation of image states from the bare substrate as well as from 1 and 2 ML high Au islands is clear proof for a three-dimensional growth. The solid line in Fig. 30 denotes the vacuum level which reaches its final value [*Reuß (1994)*] only at relatively high coverages. The slow non-linear increase of the work function is also compatible with the three-dimensional growth of Au on Cu(111). For Au coverages between 2 and 5 ML no clear identification of unoccupied image states is possible. Above 5 ML the peak characteristic for the Au(111) image state is observed.

The band gap of Cu(111) ends at 4.1 eV, which implies that the observed states on Au films are outside the Cu as well as the Au(111) band gap. One expects a behavior similar to the quantum well states for Au on Pd(111) with the difference that the reflectivity of the substrate is reduced, because a penetration of the wave

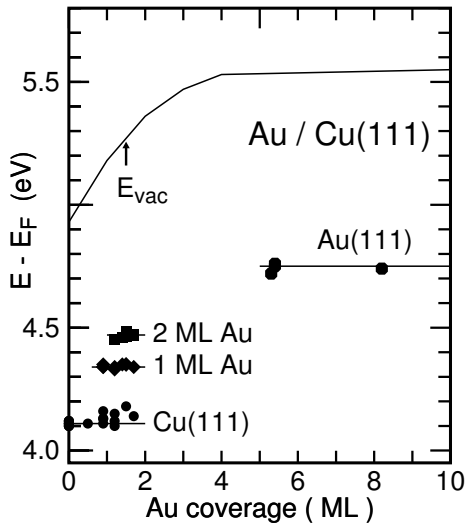

FIG. 30. Energies of the detected states relative to E_F as a function of Au coverage on Cu(111) [*Wallauer and Fauster (1995)*]. The solid line represents the vacuum level. One recognizes the $n = 1$ image state from Cu(111), the first image state from 1 and 2 ML high gold islands, as well as the first image state from thick Au islands.

function into the Cu(111) bulk is possible. The experimental binding energies of the image states for 1 and 2 ML taken from Tab. 4 are 0.84 and 0.89 eV, respectively. The latter value in particular indicates an influence of the quantum well. This interpretation has to be taken with caution, because for the three-dimensional growth the measured work function generally does not agree with the local work function at the islands of the appropriate height. Higher members of the image-state series could not be observed, making an extrapolation of the local work function impossible. Because rough surfaces exhibit a lower macroscopic work function [*Wandelt (1987)*], the binding energies might actually be larger than quoted above. The calculated energies of the image states using the measured work functions are slightly below the experimental values (Tab. 4). This supports the previous statement, but is also in accord with the general trend to underestimate the image-state energies relative to E_F outside band gaps by the one-dimensional scattering model without an imaginary part of the bulk potential. Examples for this can be found in the rows of Tab. 4 containing Au or Cu.

3. Surface morphology

The preceding section has illustrated how the local work function and the interaction with quantum well states influences the binding energies of image states on metal overlayers. The growth mode could be inferred in several examples. In this section the modification of the

growth mode and surface morphology through the variation of the sample temperature will be discussed.

1. Segregation: Co on Cu(111)

The observed image states and the measured work function is shown as a function of the deposited Co coverage on Cu(111) in Fig. 31. The $n = 1$ image state of the Cu(111) substrate can be seen for coverages up to 1.6 ML. This is an unambiguous proof for the existence of free Cu areas and a growth of three-dimensional Co islands. The Co image states do not exhibit much variation, because the state is at 1 ML already less than 0.1 eV away from the Co(0001) value. The work function also does not show significant change in the coverage regime plotted in Fig. 31. The asymptotic value of 5.20 eV has not been reached even at coverages of 14 ML where 5.16 eV was measured. Particularly noteworthy is the large scatter of the experimental data for the work function. This is in striking contrast to the other systems presented so far, which are reproducible within 0.03 eV. In those cases the work function could be used conveniently to supplement the coverage calibration. For Co on Cu(111) the large scatter indicates a critical influence of the details of the preparation conditions. This is in accord with the contradictory results about the growth mode obtained for this system even in recent years. Some researchers find evidence for three-dimensional island growth [*Kief and Egelhoff, Jr. (1993), Figuera et al. (1993), Harp et al. (1993), Fauster et al. (1993)*] while other groups favor the layer-by-layer growth mode [*Gonzalez et al. (1981), Chen et al. (1991), Tonner et al. (1993)*]. A very critical dependence of the growth mode on the adsorption conditions such as temperature and deposition rate has been proven recently [*Rabe et al. (1994)*].

The instability of this system can be seen from the

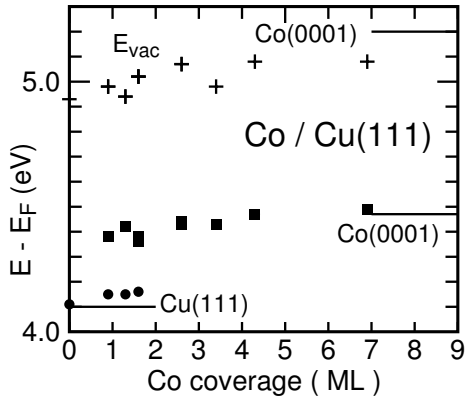

FIG. 31. Work function and energies of the detected image states relative to E_F as a function of Co coverage on Cu(111) [*Wallauer and Fauster (1995)*].

2PPE results of annealing experiments [*Wallauer and Fauster (1995)*] for Co on Cu(111). The energies of the detected states after annealing at the indicated temperatures for 60 s are plotted in Fig. 32 for three different Co coverages. The solid lines labeled E_{vac} denote the vacuum level and the different symbols stand for different coverages. After annealing the 1.6 ML film to 370 K, a peak at an energy between the image states of the substrate and the deposited film appears (filled symbols in Fig. 32). Further annealing leads to increases in the relative intensity of this peak. At 870 K the image state of the clean Cu(111) surface is retrieved. Simultaneously with the appearance of the new peak, a drastic drop of the vacuum energy towards the value of a clean Cu(111) surface is observed. The new peak is assigned to the $n = 1$ image state of 1.6 ML Co on Cu(111) on which copper has segregated. This interpretation also explains that for thicker cobalt films it takes higher temperatures to achieve the detection of the new peak (see Fig. 32). For higher coverages segregation is slower, either because less Cu is exposed to the surface, or because Cu has to diffuse through a thicker Co film.

The annealing experiments reveal the segregation of copper onto the cobalt islands, because the resulting Cu/Co/Cu(111) $n = 1$ image peak can be resolved from

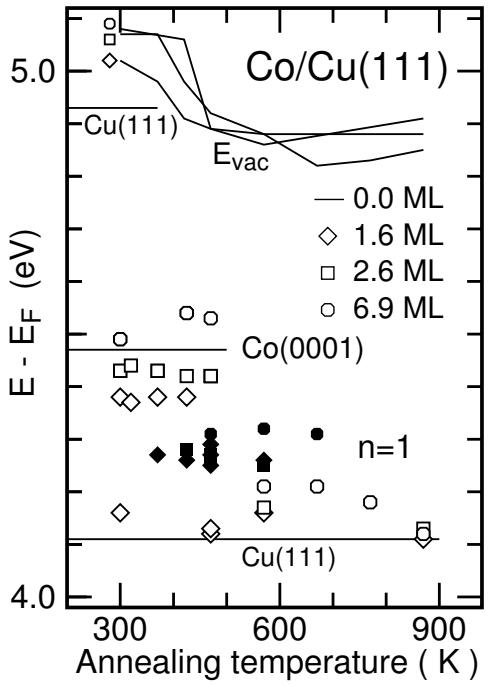

FIG. 32. Energies of the detected image states relative to E_F as a function of the annealing temperature for Co on Cu(111) [*Wallauer and Fauster (1995)*]. The solid lines represent the vacuum level and the bulk values of the $n = 1$ image state, respectively. One clearly sees the appearance of additional states (filled symbols) already at low annealing temperatures.

the $n = 1$ image peak of the cobalt islands and the Cu(111) substrate. The segregation of a single layer of Cu onto the Co film is supported by calculations within a one-dimensional scattering model [*Fauster (1994)*]. Because at least two peaks are observed in the temperature range where the additional state appears, the surface is presumably rather inhomogeneous. This makes the choice of the local work function for the calculations somewhat arbitrary and the results less assertive. Previous reports have also suggested the presence of copper atoms on top of the cobalt islands [*Fauster et al. (1993)*] and found evidence for the migration of copper atoms already during the evaporation process at room temperature [*Rabe et al. (1994)*]. The onset of significant segregation of Cu onto thin Co films above 350 K has been observed in other studies [*Chen et al. (1991), Rabe et al. (1994)*].

2. Alloy formation: Ag on Pd(111)

For Ag deposited at room temperature a layer-by-layer growth has been reported in Sect. 5 1 1. The growth mode may change at lower temperature when the diffusion of the arriving Ag atoms is reduced and the island formation is inhibited. As an example [*Fischer et al. (1993b), Fischer and Fauster (1996)*], spectra for 1.0 ML of Ag on Pd(111) are presented in Fig. 33. The lowest spectrum for deposition at 90 K shows two series of image states, and looks similar to the one for 1.35 ML of Ag on Pd(111) in Fig. 20. The series at lower energy comes from two-layer-thick Ag areas, and the other from one-layer-thick areas. Because the coverage is 1 ML patches which are not covered by Ag must also exist on the surface. The image states of the clean Pd(111) substrate are not seen in Fig. 33 because they lie above the measured vacuum energy. The photon energies $2h\nu$ have to be lower than the work function Φ to avoid one-photon photoemission. At lower temperature the mobility of the Ag atoms is reduced, and a change of the growth mode to three-dimensional islands occurs, as sketched in the bottom of Fig. 33. The observation of the image states requires a certain size of the islands (see Sect. 5 3 3). This implies that at 90 K the diffusion on the terraces is still significant and mainly the diffusion over island edges is inhibited [*Günther et al. (1993)*].

The spectra show pronounced changes after heating the sample for 60 s to the temperatures given in Fig. 33 and subsequent cooling down to 90 K for the measurements. After heating just above room temperature, the series at lower energies has disappeared and only electrons from one-layer-thick Ag areas are observed. The spectrum for 373 K is similar to the one where 1 ML of Ag is deposited at room temperature (compare to Fig. 20). The Ag atoms have covered the open Pd(111) patches

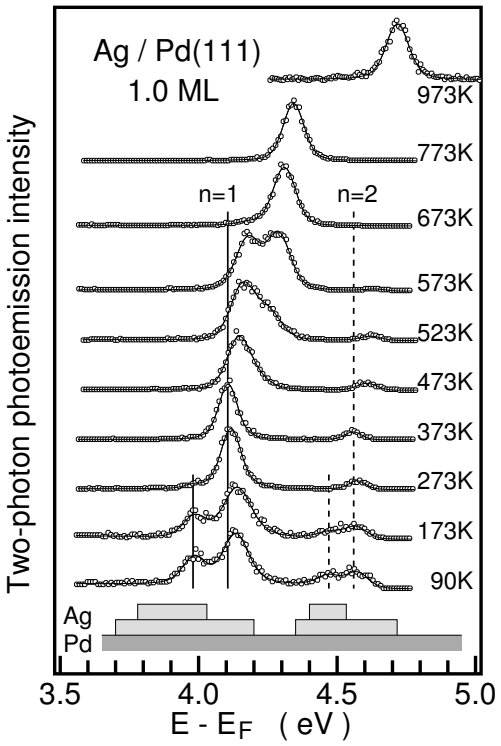

FIG. 33. Two-photon photoemission spectra for 1 ML Ag on Pd(111) deposited at 90 K and after heating to the indicated temperatures for 60 s [*Fischer et al. (1993b)*]. The energy scale is relative to E_F.

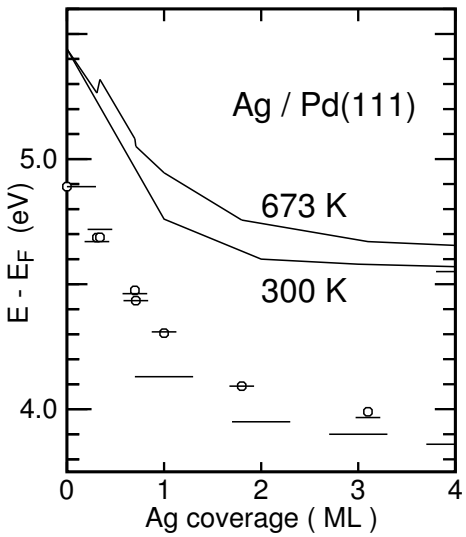

FIG. 34. Vacuum level (solid line) and energies of the detected image states relative to E_F (open symbols) after annealing of Ag films on Pd(111) to 673 K [*Fischer et al. (1993b)*]. The short lines show the result of a calculation for a homogeneous surface alloy. Dashed lines give the corresponding quantities for films as deposited at 300 K (compare to Fig. 21).

and the Ag film forms a smooth layer.

For heating temperatures above 500 K the image state gets broader and shifts to higher energy. At about 600 K one narrow peak is observed, which does not shift in energy up to about 750 K. Due to the narrow symmetric lineshape, it must be an image state on a homogeneous surface. Because its energy is between the values for 1 ML of Ag and clean Pd, it must be due to a surface alloy. The stable surface alloy between 600 K and 750 K is observed for coverages up to 16 ML. The energies of the image states shown by the open symbols in Fig. 34 are always higher than the corresponding values for completed layers after deposition at room temperature (dashed lines). Calculations with the one-dimensional scattering model (short horizontal lines in Fig. 34) show excellent agreement with the experimental values, especially at small coverages where the fractional Ag coverage is used as concentration x in Eq. 13. A monolayer confined mixing has been found for Ag on Pt(111) at similar temperatures [*Röder et al. (1993b), Strüber and Küppers (1993)*].

For annealing temperatures above 750 K the image state shifts further in the direction of the clean Pd(111) surface (Fig. 33 and [*Fischer and Fauster (1996)*]). The Ag evaporates or gets incorporated deeper into the bulk. At about 1200 K the image states and the work function of the clean Pd(111) surface are observed.

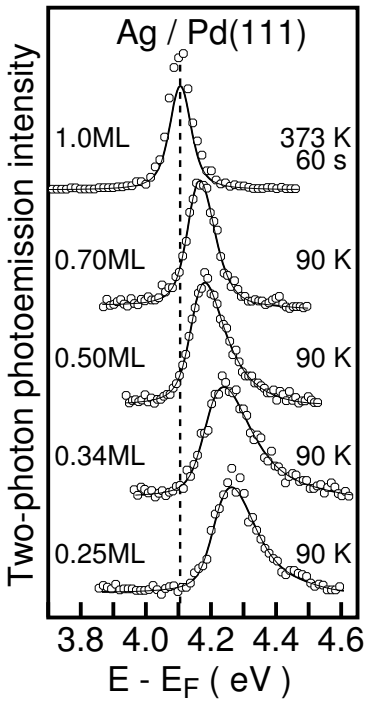

FIG. 35. Two-photon photoemission spectra for various amounts of Ag on Pd(111) deposited at 90 K. The energy shift relative to a smooth film (dashed line) is due to the lateral localization of the image state [*Fischer et al. (1993b)*].

3. Islands: Ag on Pd(111)

The most important result obtained from the data for Ag on Pd(111) is that the image-state series for the bare Pd substrate and Ag layers of different height can be easily distinguished due to their different energies. This has been used in the preceding section to identify the growth of three-dimensional islands at low temperatures. The concept of the local work function leads to the unambiguous assignment of electrons to patches of different Ag coverage. This means that they are localized laterally on the surface in addition to the perpendicular direction. This section deals with the following questions: What is the minimum size of an island which can support image states and can effects of the lateral localization be observed?

The experimental answer to these questions requires the preparation of small Ag islands which can be achieved for small coverages deposited at low temperatures. In Fig. 35 spectra for Ag coverages between 0.25 and 0.7 ML adsorbed at 90 K are shown [*Fischer et al. (1993b)*]. A shift of up to 0.2 eV to higher energy compared to the case of a smooth 1 ML Ag film (top spectrum and dashed line in Fig. 35) is observed. The width of the peaks is larger than for image states on homogeneous surfaces and the lineshape is asymmetric with a tail at the high-energy side. At these low coverages no significant occupation of two-layer-high islands is expected and there is no intensity to the left of the peaks (compare to Fig. 33).

The energy shifts are due to the lateral confinement of the image-state electrons on the Ag islands. This situation is illustrated in Fig. 36. For an electron localized in the lateral dimension, the wave function is shown by the thin solid line. The bottom of the potential well is given by the energy of the $n = 1$ image state for one layer of Ag on Pd(111). The well has a finite height limited by the energy of the $n = 1$ state for clean Pd(111). This choice of the parameters for the potential well yields the correct limiting values for vanishing and infinite island diameter x. The energy of a particle in a square infinitely-high box of area x^2 is

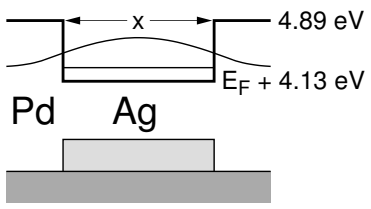

FIG. 36. Energy shift (dotted line) and the wave function for a image state localized on a small Ag island.

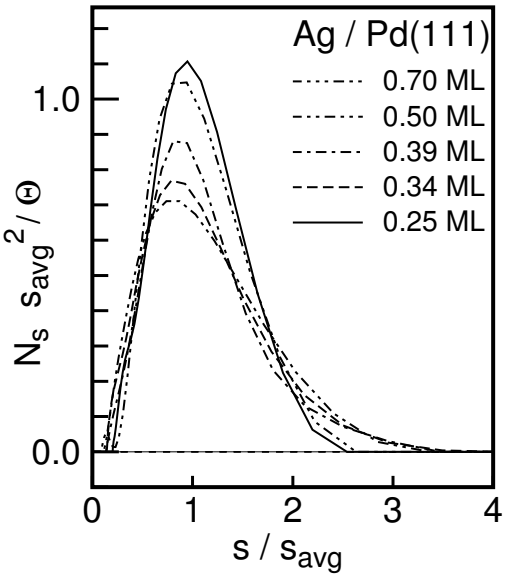

FIG. 37. Number of islands N_s of islands with s atoms derived from the experimental data of Fig. 35. The curves agree well if scaled with the average number s_{avg} and the coverage Θ [*Bartelt and Evans (1993)*].

$$\Delta E = 2\,\hbar^2\pi^2/2mx^2\ . \tag{25}$$

Islands on hexagonal substrates are not expected to be squares, but the energy shift is inversely proportional to the area for other shapes as well with a different proportionality factor in Eq. 25. The energy shift for localization in one dimension on a stripe of width x is half the value given in Eq. 25. This implies that Eq. 25 holds within a factor of the order of two even for islands of fractal or ramified shape as observed by scanning tunneling microscopy [*Günther et al. (1993), Röder et al. (1993a)*]. The finite depth of the potential well leads to a smaller prefactor in Eq. 25. This correction depends only weakly on the island shape and is valid for the energy shifts used in this work which are small compared to the well depth.

The consequence of Eq. 25 is that the island area can be derived from the energy shift and that the shape of the spectra in Fig. 35 reflects the distribution of island areas. Using a least-square-fit procedure the distribution of the islands sizes has been obtained from the experimental spectra [*Fischer et al. (1993b)*]. Circular islands have been assumed and the potential well of finite depth shown in Fig. 36 has been used. The distributions of the number of islands N_s containing s atoms are shown in Fig. 37. The solid lines in Fig. 35 show the fits of the model to the experimental data. The distributions are normalized with the average number of atoms s_{avg} and the coverage Θ. This implies a scaling behavior and all distribution should fall on one curve [*Bartelt and Evans (1993), Ratsch et al. (1994)*]. This is approximately the case for the data of Fig. 37. Very small islands are not seen in the experimental distributions, because the energy shift would be too large and also the coverage and, consequently, the intensity would be rather small.

Mean island diameters of 20 and 40 Å are obtained for coverages of 0.25 and 0.70 ML, respectively [*Fischer et al. (1993b)*]. The mean area of the islands grows proportionally to the coverage, as can be seen from the fact that the maxima of the distributions occur around $s/s_{avg} = 1$ in Fig. 37. This behavior can be explained if the density of nucleation centers is constant (in the coverage range studied here) and fixed by the experimental conditions, such as evaporation rate and temperature. A density of nucleation centers of 7×10^{12} cm^{-2} is obtained at 90 K. This corresponds to a diffusion length of ≈ 20 Å, in agreement with other work [*Günther et al. (1993), Röder et al. (1993a)*].

4. Alkali metal overlayers

Alkali metals have the lowest work function of all elements and a large work-function change occurs upon the deposition of submonolayer coverages of alkali overlayers on noble or transition-metal substrates. A study of the image states should, therefore, reveal whether they exist over the whole coverage regime and whether the concept of the local work function can be extended to a case with a large work-function difference between the substrate and the overlayer.

1. Proper work function of monolayers

To address these problems it is appropriate to study the case of homogeneous surfaces covered with one monolayer of alkali metals first. Two-photon photoemission spectra of the unoccupied states have been measured for 1 ML coverage of K on Fe(110) and Cu(111) and of Na on Cu(111), Co(0001), and Fe(110) [*Fischer et al. (1993a)*], and are shown in Fig. 38 on an energy scale referred to E_F. Up to three unoccupied states can be seen and are assigned to the image states on these surfaces. The upper three spectra in Fig. 38 show a strong 2PPE signal of the $n = 3$ image state, because the photon energy was chosen for resonant excitation between the occupied alkali-induced state and this state [*Fischer et al. (1991)*]. Common features of the spectra in Fig. 38 are the same energies relative to E_F of the image states for the same adsorbate independent of the substrate and the identical energy differences between image states, regardless of substrate or adsorbate. The widths of the image states are also similar, but considerably larger (> 0.14 eV [*Fischer et al. (1993a)*]) than on the clean surfaces (compare Fig. 16 and Tab. 3). The measured work function is indicated by the arrows in Fig. 38 and shows a large variation of almost 0.2 eV for the same adsorbate. With the energy

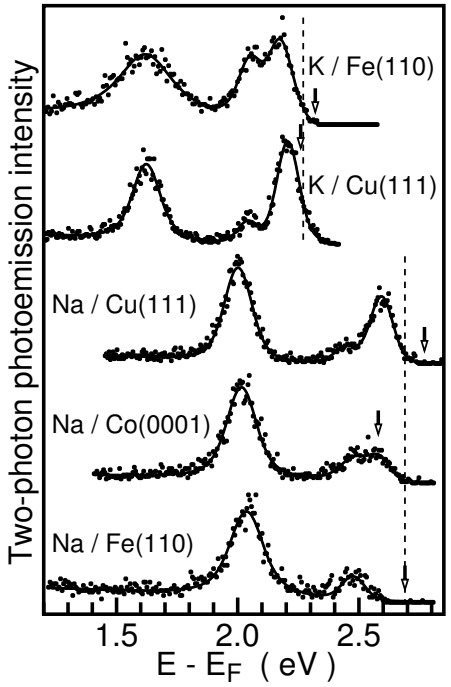

FIG. 38. Two-photon photoelectron spectra for a single layer of Na and K on different substrates [*Fischer et al. (1993a)*]. For each system a series of unoccupied states can be seen. The arrows mark the measured work function and the dashed lines the extrapolated work function.

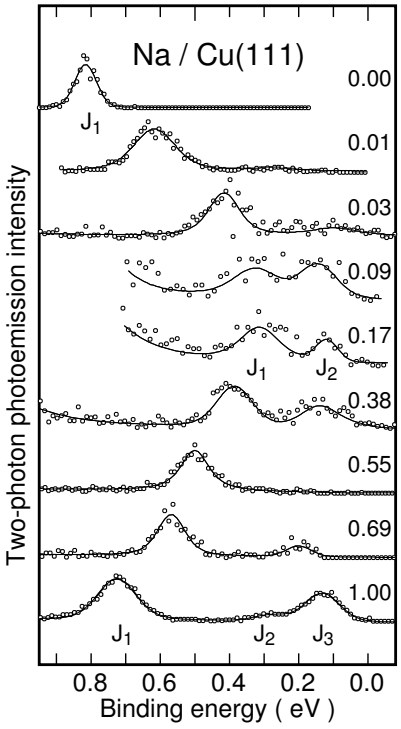

FIG. 39. Series of two-photon photoemission spectra showing the image states for Na on Cu(111) at the coverages (ML) given to the right of each spectrum [*Fischer et al. (1994)*].

of the image states fixed this leads to a contradiction, because the image states should be pinned energetically to E_{vac}.

The solution to this problem can be found with the help of the quantum-defect formula, which has worked extremely well for the clean homogeneous surfaces discussed so far. Using the measured image-state energies and Eq. 15 the extrapolated work functions shown by the dashed lines in Fig. 38 are obtained. The difference to the work functions measured at the low-energy cutoff can be explained only if the prepared monolayers are not homogeneous surfaces, but contain defects like islands of different height or contaminants [*Fischer et al. (1993a)*]. The relatively large linewidths indicate a certain amount of imperfection on the alkali-covered surfaces.

2. Coverage dependence of image states

Two-photon photoemission spectra for Na on Cu(111) are shown in Fig. 39 for coverages between 0 and 1 ML [*Fischer et al. (1994)*]. The data are presented on a binding energy scale in order to eliminate the large shifts relative to E_F caused by the work-function change of 2.75 eV. The assignment of the peaks J_n to image states is demonstrated by the observation of a series of states converging towards the vacuum level for most spectra. The width of the image states stays quite narrow at all coverages. The binding energy of the image states J_1 relative to E_{vac} changes continuously with coverage. Around 0.2 ML a minimum of $\approx$ 0.3 eV is reached. This value is quite low compared to the clean surface (0.83 eV) or the monolayer (0.72 eV).

The compilation of all data for the image states is presented in Fig. 40. The vacuum energy is plotted as a solid line because the experimental data exhibit a scatter not much larger than the width of the line. The quantum-defect model Eq. 15 would suggest to assign $n = 2$ to the J_1 state around 0.2 ML. The convergence behavior of the series of states is indicated by the short lines in Fig. 40. The extrapolated work function agrees well with the measured work function, supporting the assignment above which was derived originally from the continuous evolution with coverage. The explanation for these low binding energies is not clear and might be related to an influence of the alkali states of the following section.

The energies of the image states (relative to E_F) stay almost constant for coverages below 0.025 ML (see inset in Fig. 40). This behavior contradicts the usual picture of image states pinned to the vacuum level. The work function changes by 0.58 eV, whereas the energy of J_1 changes only by 0.15 eV. This implies a shift of the binding energy by 0.43 eV, a reduction by a factor of two. The obvious interpretation (see Sect. 5 1) is that the

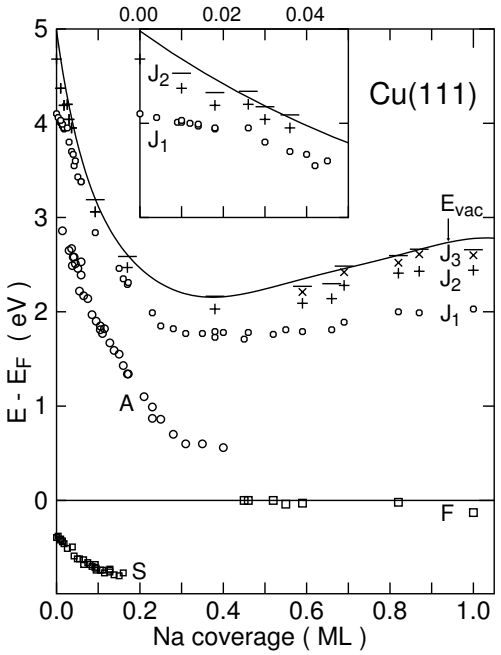

FIG. 40. Energies of the observed states for Na on Cu(111) as a function of coverage [*Fischer et al. (1994)*]. The vacuum level is indicated by the solid line and the extrapolated work function by the short lines. The inset shows the region of small coverages on an enlarged coverage scale.

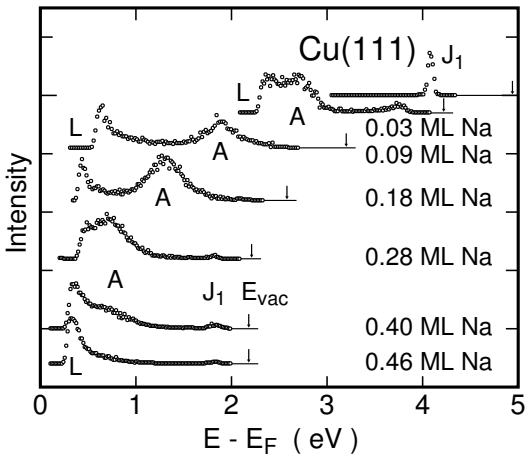

FIG. 41. Series of two-photon photoemission spectra for increasing coverage of Na on Cu(111) [*Fischer et al. (1994)*]. The energy scale is relative to E_F and the vacuum level is indicated by the arrows. The spectra are shifted downward according to the Na coverage.

image-state electrons of the copper substrate see locally the Cu(111) work function.

For coverages above $\approx$ 0.45 ML the measured work function shows a continuous increase. The energy of the image state J_1 also increases, but reaches the value characteristic for the completed monolayer [*Fischer et al. (1993a)*] already at a coverage of 0.8 ML (see Fig. 40). These observations are most easily explained by aggregation of Na atoms into islands. The observed image states then correspond to electrons located on these islands which have reached the density characteristic for the closed monolayer.

3. Alkali states

Two-photon photoemission spectra for coverages up to 1 ML of Na on Cu(111) are plotted in Fig. 41 relative to E_F. The distance between the low-energy cut-off L and E_{vac} (arrows in Fig. 41) is just the photon energy $h\nu$. Except for the top two spectra, monochromatic 2PPE has been employed because the low work function of the alkali-covered surfaces. For coverages smaller than ~ 0.4 ML a broad peak A is seen in Fig. 41. It is already visible at the smallest Na coverage of 0.03 ML and its energy shifts roughly as the work function. This state must be related to the Na atoms on the surface. The photon energy dependence reveals that it is unoccupied. The full width at half maximum of the peaks A is 410 ± 30 meV independent of coverage which is significantly larger than the experimental resolution (45 meV) and considerably larger than the intrinsic linewidth of image states. The line shape of the peaks A cannot be fitted by a Lorentzian convoluted with a Gaussian representing the experimental resolution which indicates that the peak width is not due to the finite lifetime of a single electronic state. Above 0.40 ML the states A are no longer visible. From 0.45 ML on, an occupied alkali-induced state F appears which has its highest intensity around the full monolayer coverage [*Fischer et al. (1993a)*]. The energy of the occupied alkali-induced state F for coverages above 0.45 ML lies within 0.11 eV below E_F. The occupied state has a much narrower width of $\approx$ 100 meV. The transition from the observation of the unoccupied state A to the occupied state F is abrupt as can be seen from the energies plotted as a function of coverage in Fig. 40 (large open circles and squares).

The surface state S of the clean Cu(111) surface (see Figs. 5 and 6) shifts down in energy after the adsorption of alkali atoms (see small open squares in Fig. 40). Above a coverage of 0.16 ML the state S is no longer visible, presumably because its energy would be outside the band gap (see Tab. 1). It could continue to exist as a surface resonance, but it is no longer observed by the photoemission experiments.

4. Discussion

The alkali state A presented in the preceding section is the first example in this chapter of a state observed by two-photon photoemission which is not an image state.

The high resolution, the sensitivity, and the low background of 2PPE permitted the identification of the unoccupied alkali state A even at very low coverages. The image states J exist independently of the alkali state A and are located more than 0.9 eV higher in energy. The 2PPE results for other alkali adsorption systems are very similar [*Fischer et al. (1993a), Fischer et al. (1994)*]. The distinction between alkali states and image states disproves several inverse photoemission studies as discussed in Ref. [*Fischer et al. (1994)*]. A 2PPE study for K on Ag(100) found an alkali state but no image states [*Nielsen and Thowladda (1993)*]. The alkali state undergoes an abrupt transition from unoccupied to occupied at an coverage slightly above the work-function minimum. This transition might be correlated with the transition from an ionic to a metallic state of the alkali atoms on the surface [*Fischer et al. (1994)*].

In model calculations the alkali layer is often represented by a square potential [*Lindgren and Walldén (1988), Memmel et al. (1991), McNeill and Harris (1993)*]. A variation of the depth [*Lindgren and Walldén (1988)*] or the width [*Memmel et al. (1991)*] of the potential well is used to describe the coverage dependence. Such calculations predict a continuous transition from the image state J_1 of the clean surface to the occupied state F just below E_F at the full monolayer coverage [*Lindgren and Walldén (1992)*]. The observation of well-separated alkali-induced states and image states at low coverages disproves this picture and makes the use of such simple model calculations questionable. A proper description of the alkali-derived states at low coverages has to take the atomic orbitals of the alkali atoms into account which cannot be replaced by a square well.

Particularly surprising is the fact that the energy of the unoccupied alkali state A does not depend on the alkali species within the experimental uncertainty. The extrapolated work function also is independent of the substrate [*Fischer et al. (1993a)*]. Theoretical work for jellium [*Lang (1971)*] predicted this as long as the effective electron density is constant, which is the case for the monolayers with their close-packed structures.

6. IMAGE STATES ON DIELECTRIC OVERLAYERS

For the surface of a dielectric material, the screening is much less effective and the image force is reduced. The boundary conditions for the electric field are changed and the potential Eq. 2 is reduced by a factor $(\epsilon - 1)/(\epsilon + 1)$ where ϵ is the dielectric constant. This leads to a corresponding reduction of the binding energies. In fact, the first observation of image states was on the surface of liquid helium [*Cole and Cohen (1969), Leiderer (1992)*]. For dielectric overlayers on a metal substrate, a somewhat smaller reduction of the binding energy is expected. Other effects as changes of the effective mass or lifetime may occur as well. The electronic structure of the adsorbate might lead to the observation of additional (non-image) states.

1. Rare gases: Xe

The ideal dielectric adsorbates are thin layers of rare gases. The first system studied were the image states for a monolayer of Xe on Ag(111) [*Padowitz et al. (1992), Merry et al. (1993)*]. A reduction of the binding energy from 0.76 eV to 0.67 eV has been found, which is in accord with the lowering of the work function by 0.45 eV and the resulting change of the energetic position relative to the band gap (see Fig. 18). This implies a reduced penetration into the metal which explains the smaller linewidth observed on the Xe monolayer compared to the clean surface. The position of the image plane outside the Xe layer [*Merry et al. (1993)*] leads to a further reduction of the penetration. The dispersion goes down upon adsorption and is described by the free-electron mass compared to 1.3 m for Ag(111). This effect can only partially be accounted for by the energy being further away from the band gap (see Sect. 4 2) and is not yet fully understood.

2. Diatomic Molecules

In most cases the image states disappear after saturation of clean metal surfaces with molecular adsorbates [*Rieger et al. (1987), Kubiak (1987), Hamza and Kubiak (1990), Schuppler et al. (1990a), Schuppler et al. (1992), Padowitz et al. (1992), Wallauer (1993)*]. The reason is the reduced lifetime of the states which shows up in a linewidth broadening at submonolayer coverages [*Schuppler et al. (1992)*]. An example is shown in Fig. 42 where 2PPE spectra for different coverages of CO adsorbed at room temperature are plotted [*Wallauer (1993)*]. The image state shifts relative to E_F with increasing number of CO molecules on the surface and significantly broadens at the same time. At coverages > 0.25 ML the image state is no longer visible.

The adsorbate-induced shifts of the binding energy and lifetime are shown in Fig. 43 [*Wallauer (1993)*]. The binding energy shows a linear increase with coverage, in contrast to the simple expectation for a dielectric overlayer. The increase of the work function and the associated change of the energetic position in the Pd(111) band gap explains only $\sim 10\%$ of the observed binding energy increase. Therefore, a significant modification of the surface potential by the adsorbate must occur. Similar effects but of different magnitude are observed for CO or O_2 adsorbed at 100 K and atomic oxygen at room temperature on Pd(111) [*Wallauer (1993)*]. For O / Cu(100)

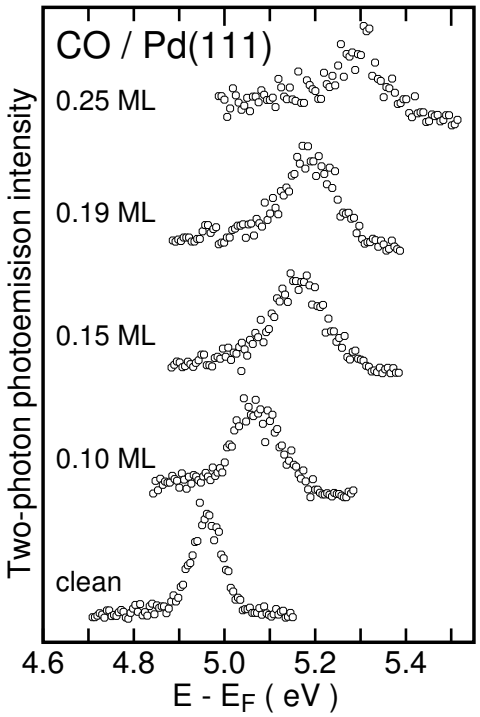

FIG. 42. Series of two-photon photoemission spectra for increasing coverage of CO on Pd(111) [*Wallauer (1993)*]. The energy scale is relative to E_F and the coverage is shown on the left.

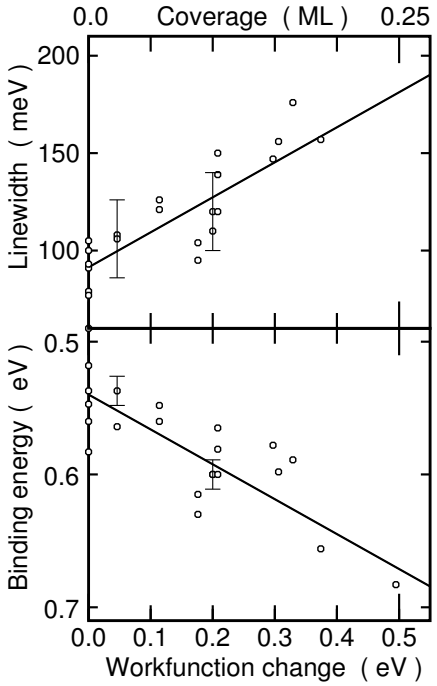

FIG. 43. Adsorbate-induced changes of the binding energy and the linewidth of the first image state $n = 1$ for CO on Pd(111) [*Wallauer (1993)*]. The straight lines are least-squares fits to the data.

no change of the binding energy has been reported [*Wu et al. (1992)*].

The linewidth broadening of the image state can be explained by two contributions which are both proportional to the coverage [*Schuppler et al. (1992)*]. These are inelastic scattering of the electron out of the image state by adcenters and elastic scattering of the electron at confining adcenters. The first effect directly reduces the lifetime. The elastic scattering reduces the lateral extension of the image state which leads to a $k_{\|}$ uncertainty. This leads to an energy uncertainty [*Schuppler et al. (1992)*] and a slope for the elastic broadening of about 0.58 eV/ML is obtained for Pd(111). In most cases a larger effect is found, indicating an additional contribution by inelastic scattering [*Schuppler et al. (1992), Wallauer (1993)*]. For CO adsorbed on Pd(111) at room temperature, the broadening was found to have a smaller slope than expected. This might be explained by an elastic reflection coefficient < 1 or by the formation of CO islands [*Hoffmann (1983)*] leading to a reduction in the number of scattering centers.

On Cu(111) adsorbate states have been also investigated. For oxygen an occupied state at -2.13 eV and an unoccupied state at 2.79 eV relative to E_F have been observed [*Rieger et al. (1987)*]. An occupied NO state was detected at -2.3 eV and a broad unoccupied state 1.3 eV above E_F was reported [*Munakata et al. (1993)*]. The $2\pi^*$ orbital of CO was measured 3.35 eV above E_F and was found to exhibit no dispersion [*Hertel et al. (1994)*]. For other systems only occupied adsorbate states have been detected [*Rieger et al. (1987), Hamza and Kubiak (1990)*].

3. Larger Molecules: Alkanes

A variety of larger molecules on Ag(111) has been studied with two-photon photoemission by the group of Harris. In most cases a quenching of the image states has been observed [*Padowitz et al. (1992)*]. For alkane overlayers the image states persisted and several image states from different layers could be identified and resolved [*Lingle et al. (1994)*]. For monolayers and the $n = 2$ state the dispersion could be described by the free-electron mass. For the $n = 1$ image states on bilayers and trilayers of straight chain alkanes an effective mass 1.2 times higher was found. The observation of dispersionless features is attributed to the localization of electrons at interfaces [*Lingle et al. (1994)*].

7. CONCLUSIONS

The examples in the chapter have illustrated that electrons in image states are localized in front of metal sur-

faces and how they can be used to probe the properties of the surface. For clean surfaces the binding energy and lifetime give information on the energetic position of the band gaps relative to the image-state energy. Localization in the overlayer or on small islands can be observed for metal overlayer systems. Dielectric adsorbates are still less understood. The image-state electrons are not involved in metallic or chemical bonds and couple only weakly to the electronic states of the sample. This makes them the ideal test electrons for the surface electronic structure. Two-photon photoemission provides the experimental basis for the investigation of image states with high energy resolution and low background.

ACKNOWLEDGMENTS

We have benefitted from the excellent experimental work and the ideas of N. Fischer, R. Fischer, K. Giesen, F. Hage, S. Schuppler, and W. Wallauer. Additional contributions came from Chr. Reuß, D. Rieger, H. J. Rieß, and Th. Wegehaupt. F. J. Himpsel initiated the application of two-photon photoemission spectroscopy to the study of image states. This work would not have been possible without the continuous support by the Deutsche Forschungsgemeinschaft.

---

de Andres, P., P. M. Echenique and F. Flores, 1987, Phys. Rev. B **35**, 4529.

Ashcroft, N. W., and N. D. Mermin, 1976, *Solid State Physics* (Saunders College, Philadelphia), Chap. 8, Problem 1.

Bartelt, M. C., and J. W. Evans, 1993, Surf. Sci. **298**, 421.

Borensztein, Y., T. Lopez-Rios and G. Vuye, 1987, Phys. Rev. B **37**, 6235.

Borstel, G., and G. Thörner, 1988, Surf. Sci. Rep. **8**, 1.

Bulović, V., B. Quiniou and J. R. M. Osgood, 1994, J. Vac. Sci. Technol. A **12**, 2201.

Chambliss, D. D., and R. J. Wilson, 1991, J. Vac. Sci. Technol. B **9**, 928.

Chen, Q., M. Onellion and A. Wall, 1991, Thin Solid Films **196**, 103.

Cole, M. W., and M. H. Cohen, 1969, Phys. Rev. Lett. **23**, 1238.

Dose, V., W. Altmann, A. Goldmann, U. Kolac and J. Rogozik, 1984, Phys. Rev. Lett. **52**, 1919.

Eberhardt, W., and E. W. Plummer, 1980, Phys. Rev. B **21**, 3245.

Echenique, P. M., and J. B. Pendry, 1978, J. Phys. C **11**, 2065.

Echenique, P. M., and J. B. Pendry, 1990, Prog. Surf. Sci. **32**, 111.

Echenique, P. M., F. Flores and F. Sols, 1985, Phys. Rev. Lett. **55**, 2348.

Eguiluz, A. G., and W. Hanke, 1989, Phys. Rev. B **39**, 10433.

Eisenhut, B., Dissertation, Universität München, 1992.

Eisenhut, B., J. Stober, G. Rangelov and Th. Fauster, 1993, Phys. Rev. B **47**, 12980.

Fauster, Th., 1994, Appl. Phys. A **59**, 639.

Fauster, Th., G. Rangelov, J. Stober and B. Eisenhut, 1993, Phys. Rev. B **48**, 11361.

de la Figuera, J., J. E. Prieto, C. Ocal and R. Miranda, 1993, Phys. Rev. B **47**, 13043.

Fischer, R., Dissertation, Universität München, 1993.

Fischer, R., and Th. Fauster, 1995, Phys. Rev. B **51**, 7112.

Fischer, R., and Th. Fauster, 1996, Surf. Rev. Lett. **3**, 1783.

Fischer, N., S. Schuppler, Th. Fauster and W. Steinmann, 1990, Phys. Rev. B **42**, 9717.

Fischer, N., S. Schuppler, R. Fischer, Th. Fauster and W. Steinmann, 1991, Phys. Rev. B **43**, 14722.

Fischer, R., N. Fischer, S. Schuppler, Th. Fauster and F. J. Himpsel, 1992, Phys. Rev. B **46**, 9691.

Fischer, N., S. Schuppler, R. Fischer, Th. Fauster and W. Steinmann, 1993a, Phys. Rev. B **47**, 4705.

Fischer, R., Th. Fauster and W. Steinmann, 1993b, Phys. Rev. B **48**, 15496.

Fischer, R., S. Schuppler, N. Fischer, Th. Fauster and W. Steinmann, 1993c, Phys. Rev. Lett. **70**, 654.

Fischer, N., S. Schuppler, Th. Fauster and W. Steinmann, 1994, Surf. Sci. **314**, 89.

Fuggle, J. C., and J. E. Inglesfield, Eds., 1992, *Unoccupied Electronic States*, *Topics in Applied Physic 69*, (Springer, Berlin).

Fujinaga, Y., 1977, Surf. Sci. **64**, 751.

Giesen, K., Dissertation, Universität München, 1986.

Giesen, K., F. Hage, F. J. Himpsel, H. J. Rieß and W. Steinmann, 1985, Phys. Rev. Lett. **55**, 300.

Giesen, K., F. Hage, F. J. Himpsel, H. J. Rieß and W. Steinmann, 1986, Phys. Rev. B **33**, 5241.

Giesen, K., F. Hage, F. J. Himpsel, H. J. Rieß and W. Steinmann, 1987a, Phys. Rev. B **35**, 971.

Giesen, K., F. Hage, F. J. Himpsel, H. J. Rieß, W. Steinmann and N. V. Smith, 1987b, Phys. Rev. B **35**, 975.

Goldmann, A., W. Altmann and V. Dose, 1991, Solid State Commun. **79**, 511.

Gonzalez, L., R. Miranda, M. Salmerón, J. A. Vergés and F. Ynduráin, 1981, Phys. Rev. B **24**, 3245.

Graß, M., J. Braun, G. Borstel, R. Schneider, H. Dürr, Th. Fauster and V. Dose, 1993, J. Phys.: Condens. Matter **5**, 599.

Günther, C., S. Günther, E. Kopatzki, R. Q. Hwang, J. Schröder, J. Vrijmoeth and R. J. Behm, 1993, Ber. Bunsenges. Phys. Chem. **97**, 522.

Hage, F., Dissertation, Universität München, 1986.

Hamza, A. V., and G. D. Kubiak, 1990, J. Vac. Sci. Technol. A **8**, 2687.

Harp, G. R., S. S. P. Parkin, R. F. C. Farrow, R. F. Marks, M. F. Toney, Q. H. Lam, T. A. Rabedeau and R. J. Savoy, 1993, Phys. Rev. B **47**, 8721.

Hertel, T., E. Knoesel, E. Hasselbrink, M. Wolf and G. Ertl, 1994, Surf. Sci. **317**, L1147.

Himpsel, F. J., 1991, Phys. Rev. B **43**, 13394.

Hoffmann, F. M., 1983, Surf. Sci. Rep. **3**, 107.

Jacob, W., V. Dose, U. Kolac, Th. Fauster and A. Goldmann, 1986, Z. Phys. B **63**, 459.

Jaklevic, R. C., 1984, Phys. Rev. B **30**, 5494.
Johnson, P. D., and N. V. Smith, 1983, Phys. Rev. B **27**, 2527.
Jones, R. O., P. J. Jennings and O. Jepsen, 1984, Phys. Rev. B **29**, 6474.
Jurczyszyn, L., 1991, Surf. Sci. **259**, 65.
Kevan, S. D., Ed., 1992, *Angle-Resolved Photoemission*, Bd. 74 of *Studies in Surface Science and Catalysis*, (Elsevier, Amsterdam).
Kief, M. T., and W. F. Egelhoff, Jr., 1993, Phys. Rev. B **47**, 10785.
Kubiak, G. D., 1987, J. Vac. Sci. Technol. A **5**, 731.
Kubiak, G. D., 1988, Surf. Sci. **201**, L475.
Kuk, Y., L. C. Feldman and P. J. Silverman, 1983, Phys. Rev. Lett. **50**, 511.
Lang, N. D., 1971, Phys. Rev. B **4**, 4234.
Leiderer, P., 1992, J. Low Temp. Phys. **87**, 247.
Lindgren, S. Å., and L. Walldén, 1988, Phys. Rev. B **38**, 3060.
Lindgren, S. Å., and L. Walldén, 1992, Phys. Rev. B **45**, 6345.
Lingle, R. L., D. F. Padowitz, R. E. Jordan, J. D. McNeill and C. B. Harris, 1993, in *Localization of electrons at interfaces* (26th Symposion on quantum chemistry and biochemistry, Jerusalem).
Lingle, R. L., D. F. Padowitz, R. E. Jordan, J. D. McNeill and C. B. Harris, 1994, Phys. Rev. Lett. **72**, 2243.
McMahon, W. E., E. S. Hirschhorn and T.-C. Chiang, 1992, Surf. Sci. **279**, L231.
McNeill, J. D., and C. B. Harris, 1993, Solid State Commun. **87**, 1089.
McRae, E. G., 1979, Rev. Mod. Phys. **51**, 541.
Memmel, N., G. Rangelov, E. Bertel and V. Dose, 1991, Phys. Rev. B **43**, 6938.
Merry, W. R., R. E. Jordan, D. F. Padowitz and C. B. Harris, 1993, Surf. Sci. **295**, 393.
Mottet, C., G. Tréglia and B. Legrand, 1992, Phys. Rev. B **46**, 16018.
Munakata, T., K. Mase and I. Kinoshita, 1993, Surf. Sci. **286**, 73.
Nielsen, H. B., and W. Thowladda, 1993, Surf. Sci. **284**, L426.
Nielsen, H. B., G. Brostroem and E. Matthias, 1989, Z. Phys. B **77**, 91.
Ortega, J. E., F. J. Himpsel, G. J. Mankey and R. F. Willis, 1993, Phys. Rev. B **47**, 1540.
Ortega, J. E., F. J. Himpsel, R. Haight and D. R. Peale, 1994, Phys. Rev. B **49**, 13859.
Padowitz, D. F., W. R. Merry, R. E. Jordan and C. B. Harris, 1992, Phys. Rev. Lett. **69**, 3583.
Pendry, J. B., 1974, *Low Energy Electron Diffraction* (Academic Press, London), Chap. IIIB.
Quiniou, B., V. Bulović and J. R. M. Osgood, 1993, Phys. Rev. B **47**, 15890.
Rabe, A., N. Memmel, A. Steltenpohl and Th. Fauster, 1994, Phys. Rev. Lett. **73**, 2728.
Ratsch, C., A. Zangwill, P. Šmilauer and D. D. Vvedensky, 1994, Phys. Rev. Lett. **72**, 3194.
Reuß, Ch., Diplomarbeit, Universität München, 1994.
Rieger, D., T. Wegehaupt and W. Steinmann, 1987, Phys. Rev. Lett. **58**, 1135.
Röder, H., H. Brune, J.-P. Bucher and K. Kern, 1993a, Surf. Sci. **298**, 121.
Röder, H., R. Schuster, H. Brune and K. Kern, 1993b, Phys. Rev. Lett. **71**, 2086.
Santoni, A., and F. J. Himpsel, 1991, Phys. Rev. B **43**, 1305.
Schoenlein, R. W., J. G. Fujimoto, G. L. Eesley and T. W. Capehart, 1988, Phys. Rev. Lett. **61**, 2596.
Schoenlein, R. W., J. G. Fujimoto, G. L. Eesley and T. W. Capehart, 1990, Phys. Rev. B **41**, 5436.
Schoenlein, R. W., J. G. Fujimoto, G. L. Eesley and T. W. Capehart, 1991, Phys. Rev. B **43**, 4688.
Schuppler, S., Dissertation, Universität München, 1991.
Schuppler, S., N. Fischer, Th. Fauster and W. Steinmann, 1990a, Appl. Phys. A **51**, 322.
Schuppler, S., N. Fischer, W. Steinmann, R. Schneider and E. Bertel, 1990b, Phys. Rev. B **42**, 9403.
Schuppler, S., N. Fischer, Th. Fauster and W. Steinmann, 1992, Phys. Rev. B **46**, 13539, erratum: Phys. Rev. B **47**, 10058 (1993).
Shapiro, A. P., A. L. Wachs and T.-C. Chiang, 1986, Solid State Commun. **58**, 121.
Smith, N. V., 1985, Phys. Rev. B **32**, 3549.
Smith, N. V., and C. T. Chen, 1991, Surf. Sci. **247**, 133.
Smith, N. V., C. T. Chen and M. Weinert, 1989, Phys. Rev. B **40**, 7565.
Smith, N. V., N. B. Brookes, Y. Chang and P. D. Johnson, 1994, Phys. Rev. B **49**, 332.
Starke, K., K. Ertl and V. Dose, 1992, Phys. Rev. B **45**, 6154.
Steinmann, W., 1989, Appl. Phys. A **49**, 365.
Straub, D., and F. J. Himpsel, 1984, Phys. Rev. Lett. **52**, 1922.
Straub, D., and F. J. Himpsel, 1986, Phys. Rev. B **33**, 2256.
Strüber, U., and J. Küppers, 1993, Surf. Sci. **294**, L924.
Strupp, P. G., P. C. Stair and E. Weitz, 1993, Surf. Sci. **290**, L699.
Tonner, B. P., Z.-L. Han and J. Zhang, 1993, Phys. Rev. B **47**, 9723.
Wallauer, W. (unpublished).
Wallauer, W., Diplomarbeit, Universität München, 1993.
Wallauer, W., and Th. Fauster, 1995, Surf. Sci. **331-333**, 731.
Wandelt, K., 1987, in *Thin Metal Films and Gas Chemisorption*, P. Wißmann, Ed., (Elsevier, Amsterdam), p 280.
Wu, Z., B. Quiniou, J. Wang and J. R. M. Osgood, 1992, Phys. Rev. B **45**, 9406.
Xu, R., S. Bao and G. Liu, 1990, Surf. Sci. **234**, 335.